JUNE 1982 LRP 210/82

EXPERIMENTS ON POTENTIAL GRADIENTS IN A CURRENT CARRYING PLASMA

PART II : TURBULENCE

Ch. Hollenstein and M. Guyot

Experiments on potential gradients in a current carrying plasma. Part II : Turbulence

Ch. Hollenstein and M. Guyot

Centre de Recherches en Physique des Plasmas
Association Euratom - Confédération Suisse
Ecole Polytechnique Fédérale de Lausanne
CH-1007 Lausanne / Switzerland

ABSTRACT

Two different types of turbulence are observed in the presence of a large potential jump within a current carrying plasma ($v_d < v_{te}$) and are investigated by means of correlation measurements. The electron beam on the high potential side induced by the potential jump leads to the high frequency turbulence ($f \approx f_{pe}$). The unstable waves follow the dispersion relation $\omega = kv_b$ (v_b is the electron beam velocity). The low frequency turbulence ($f < f_{pi}$) observed on the low potential side could be identified as the ion acoustic turbulence and is dominated by low frequency ($f < 0.5\ f_{pi}$) waves propagating perpendicular to the electron drift.

I INTRODUCTION

The ion acoustic instability plays an important role in basic plasma physics. Recently, a lot of effort toward an understanding of the ion acoustic [1-15] instability has been made. However many problems are far from being solved. Those not yet solved are the propagation angle of the instability, the frequency and wave spectra. Furthermore, little is known about the different wave-wave and wave-particle interactions and about the particle distribution within the turbulence as well as about saturation mechanisms.

Recently, it has been discovered that the problem of ion acoustic turbulence may also be related to the problem of the formation of large potential jumps in current carrying plasmas [16,17]. Numerical simulation showed that an ion acoustic instability may induce the formation of large potential jumps. Anomalous resistivity caused by ion acoustic turbulence causes the interruption of the current which leads to the build up of a dc potential which in turn accelerates electrons further and enhances the instability and finally leads to the formation of double layers [16].

Double layers and their associated instabilities have been studied in laboratory and space plasmas [18,19]. In most of the cases the double layer has been observed in current carrying plasmas where the electron drift velocity exceeds the electron thermal velocity [20,21]. Under these circumstances, the existence of the Buneman instability [21] and the electron beam plasma instability [21,22] have been demonstrated.

In previous papers [19,23] we reported on the existence of potential jumps in a plasma with $v_d < v_{te}$. In this paper we present a detailed study of the observed instabilities under these experimental conditions. As in a recent double layer experiment [22], the electron beam formed by the electrons accelerated in passing through the potential jump induces high frequency turbulence ($f \approx f_{pe}$). This turbulence is only observed at the high potential side of the jump. On the low potential side of the jump, the detected low frequency fluctuations could be identified as ion acoustic turbulence. The ion acoustic wave is driven unstable by the current in the plasma.

Exact knowledge of the frequency spectra, the spectral density, and the angle of propagation are important in order to characterize the turbulence. Most of this information can be obtained from the experiment using correlation techniques [4,6,24]. The frequency spectra and the spectral density show a predominance of low frequency components. Moreover, the frequency spectra show a detailed fine structure. Recent calculations of the structure of the frequency spectra for plasma conditions similar to ours, show the appearance of similar fine structures [15].

The angle of propagation for low frequencies ($f < 0.5\ f_{pi}$) is found to be perpendicular to the electron drift velocity. However, higher frequency waves propagate parallel to the drift velocity. This fact agrees with recent measurements in various experiments, where no large potential jumps were observed [4,12].

The paper is divided into three sections. In Sect. II the experimental conditions and the basic plasma parameters are discussed. In addition a description of the plasma diagnostics used is presented and a detailed review of the correlation techniques included. In Sect. III the main experimental results are presented and summarized. In the last section the results are discussed and compared with other experimental work and theories.

II EXPERIMENT

A. Experimental Arrangement

The experiment is carried out in a long triple chamber plasma device. The plasma is produced in the two end sections and drifts into the grounded stainless steel central section. The plasma has embedded a uniform longitudinal magnetic field of 25 G. A current can be passed between the grids which separate the central section from the polarized end sections. The following experiments were performed with argon at a filling pressure of 4×10^{-4} Torr. The experiment is described in more detail in previous papers [19,23].

B. Diagnostics

The basic plasma parameters such as electron temperature T_e, electron density n_e, and fluctuation level $\delta n/n$ are measured using cylindrical Langmuir probes. Plane Langmuir probes are used to

measure the electron drift velocity. The upstream and downstream electron distribution functions are obtained from the differentiated characteristics of plane Langmuir probes (Ø = 2 mm). The plasma potential is monitored by hot probes. The ion temperature is measured by a one-grid electrostatic energy analyzer, the resolution of which is found to be about 0.1 eV.

The measurement of the turbulent spectra is not an easy task. The often used Langmuir probe turns out to be, in most cases, unsuitable for this type of measurement since problems arise from the electron saturation current drawn by the probe. This current induces additional low frequency noise in the neighborhood of the probe, which may considerably contribute to the measured spectra. Capacitive probes do not suffer from this drawback [25,26]. This type of probe consists of a carefully shielded small plate similar to a Langmuir probe. However, the tip is insulated from the plasma by a glass or ceramic coating. Directional capacitive probes can be made using appropriate shielding. The probe signal is detected by a commercially available high impedance probe. The frequency response of the capacitive probe is found to be flat over a wide range of frequencies (up to 600 MHz). The spectra presented are obtained by capacitive probes with a typical tip size of 3 x 5 mm.

C. Correlation measurements

Correlation measurements turn out to be a powerful method to study turbulent states. In our experiment, correlation measurements were carried out using a correlator developed by Harker et al. [24]. Figure 1 shows the basic circuitry of the instrument. Minor modifications with respect to the original apparatus have been made.

The input signals are amplified and shifted up in frequency, by means of mixers. This stage is followed by narrow band quartz filters [f_0 = 6 MHz, Δf = 14 kHz (3dB)]. Further signal processing is then performed at the central frequency f_0 of the narrow band filter. At the output of the correlator, the real and imaginary parts of the cross power spectral density is obtained. The cross power spectral density at chosen frequencies can be obtained by appropriate adjustment of the local oscillator frequency. In this configuration, correlations up to 6 MHz can be performed. Typical measurements of the cross power spectral density in the presence of ion acoustic turbulence are shown in Fig. 2.

The frequency range can be expanded toward higher frequencies, i.e., up to the electron plasma frequency (400-500 MHz). However, the spectra have to be converted downwards to lower frequencies, which implies additional modifications of the circuit. The input amplifiers must be replaced by high frequency tuned amplifiers. These tuned amplifiers serve to restrict the downshifted spectra. With an appropriate choice of components (mixers, tuned amplifiers), the range

of operation can be expanded up to the GHz range. Figure 3 shows the cross power spectral density in the presence of the high frequency turbulence as obtained with our correlator.

Changing the position of one of the probes yields a phase contour in the plane swept by both probes. The wavelengths are determined from these maps. Futhermore, if the turbulence follows a dispersion relation $\omega(k)$, the spectral density $I(k)$ is readily obtained from additional autocorrelation measurements.

In the study of turbulence, knowledge of the direction of the wave propagation is essential and can be obtained using the same correlator. A change $\Delta\phi$ in the phase in one of the channels corresponds to a time delay $t_d = \frac{1}{f} \cdot \frac{\Delta\phi}{2\pi}$. Hence, the measurements for different phase shifts yields the direction of propagation as well as to the propagation velocity. Since the signal processing is performed at a fixed frequency, the phase shift does not depend on the input signal frequency and is therefore easy to perform.

A crucial role in correlation measurements must be attributed to the probes used [4]. For the present measurements, cylindrical Langmuir probes, the tip of which is 0.13 mm in diameter and 2 mm in length, have been used. The probe within the plasma consists of a thin (0.5 mm in diameter) silver painted ceramic tube covered by an insultating layer. The probe was matched to 50 Ω, up to the probe tip. With such an arrangement, no significant perturbation of the correlation measurements could be detected.

III TURBULENCE

In this section, we present investigations of the turbulence observed in the presence of a large stationary plasma potential jump. Two different types of turbulence occur and are described in detail.

A. Electron Beam Plasma Turbulence

In the presence of a stationary potential jump a peaking of the high frequency fluctuation occurs on the high potential side, as shown in Fig. 4. This peaking takes place at the same position where intense electron heating is found. The peak frequency of the spectra is slightly less than the local electron plasma frequency. Moreover, a radial dependence of the high frequency noise is noted. In the previous paper [19], we showed that an electron beam is present only in a narrow region around the axis. The position of this electron beam agrees with the location of the maximum power detected in the autocorrelation measurements (Fig. 5).

The phase contours in Figs. 6 and 7 are obtained from correlation measurements. They clearly show the existence of only a parallel wave number $k_{\parallel}$. No indication of significant $k_{\perp}$ could be found. The direction of wave propagation coincides with the direction of the electron beam (Fig. 8).

Fig. 9a shows the dispersion relation of the axially propagating high frequency wave. The experimental points are aligned, indicating that the dispersion relation may be written as $\omega \approx kv_b$, where v_b

denotes the electron beam velocity. The phase velocity is found to be $2.1 \cdot 10^8$ cm/sec which corresponds to an electron beam energy of about 12 eV. This value agrees with the magnitude of the potential drop across the jump as shown in Fig. 9b.

These observations show that the high frequency turbulence is induced by the electron beam. This beam is formed by electrons from the low potential side passing through the jump.The thermalization length is about 10-20 cm. Therefore, within this region, intense localized electron heating is noted.

B. Ion Acoustic Turbulence

A detailed study of the low frequency fluctuations observed at the low potential side of the jump has been performed. At the low potential side of the jump, only low frequency fluctuations up to $f \approx 0.4\ f_{pi}$ are observed. This noise peaks near to the potential jump. The turbulent wave energy W normalized to the plasma energy nT_e can be obtained from the fluctuation level by $W/nT_e \approx (\delta n/n)^2$. Figure 10 shows the normalized turbulent energy W/nT_e on axis versus the distance from the polarized grid. A change of more than two orders of magnitude in W/nT_e is found.

1. Frequency spectra

Capacitive probes have been used for the measuremnt of spectra at different positions from the polarized grid. The results are presented in Fig. 11. The first two spectra have been measured on the

high potential side, the others on the low potential side of the jump. All these spectra show the predominance of low frequency fluctuations. Most of the turbulent wave energy is concentrated below $f_{pi}/2$ or even $f_{pi}/4$. The structure of these different spectra is complex. However some remarks can be made. Near the potential jump an increase in the fluctuations located between 30 and 50 kHz is noticed. Furthermore, a complicated structure emerges within this frequency range. For lower turbulent wave energy, the maximum shifts slightly toward higher frequencies. The most remarkable phenomenon is the appearance of isolated peaks even for higher frequencies.

2. Correlation measurements

In order to obtain more information on the turbulent state of the plasma, correlation measurements have been carried out. The experimental arrrangement was chosen such that measurements in the longitudinal plane (r - z) and in the plane normal to the axis (x - y) could be performed. In order to obtain data on the turbulence for various wave energies, the measurements have been made at different positions from the polarized grid. Data for $W/nT_e = 3.6 \times 10^{-3}$, 1.25×10^{-2} and 6.25×10^{-2} respectively have been obtained. The cross power spectral density for different frequency components for these values of W/nT_e are shown in Figs. 12-17. These maps give contours of constant phase of the cross power spectral density in the r-z plane. The electron drift velocity and the magnetic field $\underline{B}_0$ are oriented parallel to the z direction.

For low frequencies, the phase contours are inclined at a very small angle with respect to $\underline{B}_0$. Parallel wavelength $\lambda_{\parallel}$ of the order of 20 to 30 cm or even longer are noted. However, the perpendicular wavelength $\lambda_{\perp}$ is of the order of a few centimeters. Therefore, the instability propagates at an angle of approximately 90^0 with respect to the electron drift velocity. The same dependence has been observed even for lower values of W/nT_e.

Moreover, in some cases two modes with different perpendicular wavelengths are detected (see, for instance, Fig. 12, 100 kHz). For increasing frequencies the phase contours show decreasing parallel wavelength $\lambda_{\parallel}$. As a result, the propagation angle $[\theta = \arctan (k_{\parallel}/k_{\perp})]$ reduces to about 45^0 or even less for frequencies around $f_{pi}/2$. At intermediate frequencies, wave propagation at different angles is observed. One wave propagate nearly perpendicular, the second with an angle of about 45^0 with respect to the electron drift.

The cone angle, obtained from the phase contours for different values of the turbulent wave energy, is summarized in Fig. 18. At low turbulent energy, the low frequency waves propagate perpendicularly. For increasing turbulence levels, the frequency range of perpendicular propagating waves increases from 0.2 to 0.6 f_{pi} at $W/nT_e = 6.25 \times 10^{-2}$. In every case, the higher frequency waves propagate at an angle of about 10 to 20 deg., i.e., nearly parallel. Two modes are observed in the frequency region where the propagation changes from perpendicular to parallel. A perpendicular propagating mode and an oblique mode coexist within this frequency region.

The phase contours in the x - y plane lead to another interesting observation. The phase contours in this particular plane have been thought to be concentric circles around the axis. However, quite different phase contours are obtained such as those shown in Fig. 19. The structure has a resemblance to low order mode structures. Asymmetries in the basic parameters as well as probe perturbation cannot explain this behavior.

Changing the phase shift in one channel of the correlator gives information on the propagation direction. Such a measurement has been made at 77 cm from the polarized grid for two different frequencies. It appears that for 200 kHz ($f/f_{pi} \approx 0.2$) the waves travel in the r direction radially outwards (Fig. 20). The behavior is the same for different z. At higher frequency (400kHz, $f/f_{pi} \approx .4$), the pattern is characterized by a standing wave at the center of the device (Fig. 21). At other axial positions, we find travelling waves in the $\pm$ r-direction, separated by a region with standing waves. Near the potential jump, the high frequencies ($f \approx 0.5 f_{pi}$) propagate parallel and in the same direction as the ion beam associated to the potential jump.

3. Wave spectra

From previous phase contour measurements, the perpendicular and parallel components of the $\underline{k}$ vector are obtained. Graphs of $k_\perp$ versus $k_\parallel$ are shown in Fig. 22 for different turbulent wave energies. Basically, two different clusters of points can be seen within these

diagrams. The first region contains $\underline{k}$ vectors with large $k_\perp$ components and very small $k_\parallel$. The second region shows that unstable waves with $k_\perp \approx k_\parallel$ are present in the turbulence investigated.

The dispersion relation of the unstable waves can be used to identify the instability leading to turbulence. Fig. 23 shows the measured dispersion relation compared with the theoretical relation for the ion acoustic mode. This relation has been calculated with the T_e/T_i value determined from the independently measured quantities T_e, T_i. Good agreement between the measurements and theory is found. The unstable waves follows the dispersion relation of the ion acoustic mode exactly . No significant deviation or broadening of the measured dispersion can be observed even for high turbulent levels. The turbulence can therefore be considered as ion acoustic turbulence.

Because of these observations, we may conclude that the spectral density depends only on the wave number. This spectral density can be now determined from additional measurements of the autocorrelation (Fig. 24). Finally, the spectral density I(k) is shown in Fig. 25 which shows that the turbulence is dominated by perpendicular propagating waves. Waves with comparable $k_\perp$ and $k_\parallel$ are thought to play a less important role in the turbulence investigated.

IV DISCUSSION AND CONCLUSION

In the presence of a large, stationary potential jump within a current carrying plasma, the associated instabilities have been studied. Two different types of instabilities, namely, low ($f < f_{pi}$) and high frequency ($f \approx f_{pe}$) turbulence are observed.

The high frequency turbulence is located on the high potential side of the potential jump. The unstable mode propagates with a phase velocity of $\omega/k \approx v_b$ (v_b is the electron beam velocity) in direction of the electron beam. The electron beam is induced by the stationary potential jump. This observation may be compared with previous experiments on double layers [22]. However, in our case, the electron beam is found to be dissipated by quasi-linear effects within a short distance, within which strong, localized electron heating is observed.

The low frequency fluctuations are observed on the low potential side of the potential jump. The Buneman instability as found in typical double layer experiments can be excluded, since it is excited only for electron drift velocities comparable to the electron thermal velocity. Moreover, the most unstable frequency for this type of instability is of the order of $2^{-4/3}\ \omega_{pe}\ (m/M)^{1/3}$ which in our case corresponds to about 4 MHz. This frequency is much higher than the observed frequency $f < 1$ MHz. By means of correlation techniques, the observed turbulence is identified as the ion acoustic instability driven unstable by the current.

The observed ion acoustic turbulence has the following properties. The frequency spectra peak at low frequencies and isolated frequency peaks and fine structure are noted. Recent calculations based on the renormalized theory with plasma parameters and conditions similar to ours support this observation [15]. The correlation measurements show the dominance of perpendicular propagating low frequency waves. High frequency waves propagate nearly parallel to electron drift. This is in agreement with experiments on ion acoustic turbulence in other devices such as hollow cathode discharges [12] and in collisionless plasmas [4]. However, at present, no theory is able to explain these observations.

In the transition region of frequency $0,2 < f/f_{pi} < 0.4$ the appearance of two modes, a perpendicular and a parallel propagating wave, is found. This phenomenon is found to exist for small turbulent energy as well as for high levels. The frequency region of perpendicular propagation is enlarged with increasing turbulence level. In spite of good plasma homogenity, it is found that the phase contours in the plane perpendicular to the axis show mode like structure.

Ion acoustic turbulence is only influenced by the effects of the large potential jump within a region of about 20 to 30 cm in front of the jump. In this region, it is found that the unstable waves propagate in the direction of the ion beam. This ion beam excited by the potential jump is thermalized within this region because of its

small charge exchange length. Within this region very high fluctuation levels and localized ion heating are observed. Outside, the basic behavior of the ion-acoustic turbulence is not found to be affected by the potential jump and is governed by the discharge current as reported in previous experiments. The present study does not provide details of the mechanism for the formation of large potential jumps from ion-acoustic turbulence, however, it does demonstrate that ion-acoustic turbulence and large, stationary potential jumps can coexist.

ACKNOWLEDGMENTS

The authors wish to thank Professor E.S. Weibel, Dr. M.Q. Tran, Dr. J Vaclavik, and Dr. K Appert for many fruitful discussions.

This work was supported by the Swiss National Science Fondation, the Ecole Polytechnique Fédérale and by EURATOM.

REFERENCES

1) W. Horton and D.J. Choi, Physics Reports 49, 273 (1979)

2) R.L. Stenzel, Phys. Fluids 21, 93 (1978).

3) R.L. Stenzel, Phys. Fluids 21, 99 (1978).

4) W. Gekelman and R.L. Stenzel, Phys. Fluids 21, 2014 (1978).

5) R.L. Stenzel and W. Gekelman, Phys. Fluids 21, 2024 (1978).

6) D.B. Ilic, Phys. Fluids 20, 1717 (1977).

7) Y. Kawai, Ch. Hollenstein, and M. Guyot, Phys. Fluids 21, 970 (1978).

8) Y. Kawai and M. Guyot, Phys. Rev. Lett. 39, 1141 (1977).

9) M. Bitter and P.J. Paris, Phys. Fluids 21, 609 (1978).

10) R.E. Slusher, C.M. Surko, D.R. Moler, and M. Porkolab, Phys. Rev. Lett. 36, 674 (1976).

11) R.E. Slusher and C.M. Surko, Phys. Fluids 23, 472 (1980).

12) B.F.M. Pots, J.J.H. Conmans, and D.C. Schram, Phys. Fluids 24, 517 (1981).

13) K. Appert and J. Vaclavik, Phys. Fluids 22, 454 (1979).

14) W. Horton Jr. and D.I. Choi, Phys. Rep. 49, 275 (1979).

15) W. Horton Jr. and D. Brock, Phys. Fluids 24, 509 (1981).

16) T. Sato and H. Okuda, Phys. Rev. Lett. 44, 740 (1980).

17) T. Sato and H. Okuda, J. Geophys. Res. 86, 3357 (1981)

18) S. Torvén in Wave Instabilities in Space Plasmas, edited by P.J. Palmadesso and K. Papadopoulos (D. Reidel, Dordecht, 1979), Vol. 74, p. 109

19) Ch. Hollenstein and M. Guyot (previous paper).

20) B.H. Quon and A.Y. Wong, Phys. Rev. Lett. 37, 1393 (1976).

21) P.Leung. A.Y. Wong, and B.H. Quon, Phys. Fluids 23, 992 (1980).

22) S. Torvén and L. Lindberg, Appl. Phys. 13, 2285 (1980).

23) Ch. Hollenstein and M. Guyot, Phys. Rev. Lett. 45, 2110 (1980).

24) K.J. Harker and D.B. Ilic, Rev. Sci. Instrum. 45, 1315 (1974).

25) J.A. Schmidt, Rev. Sci. Instrum. 39, 1297 (1968).

26) J.R. Roth and W.M. Krawczonek, Rev. Sci. Instrum. 42, 589 (1971).

FIGURE CAPTIONS

Fig. 1. Block diagram of the analog cross power spectrum analyzer. A_1 preamplifiers (for $f > f_0$, narrow band turned amplifiers), F_1 variable pass band filters, Mi Mixers, LO Local oscillator, F_2 narrow IF bandpass quarz filters (fo = 6MHz), A2 amplifier, Mu multiplier, PS 90^0 phase shifter, A_3 amplifier.

Fig. 2. Typical measurements of the cross power spectral density for different frequencies (ion plasma frequency $f_{pi} \approx 1$ MHz). The stationary probe is located at $\Delta r = 0$ mm and $\Delta z = 25$ mm. The measurements are taken at a distance of 113 cm from the biased grid.

Fig. 3. Typical measurements of the cross power spectral density for different frequencies. (electron plasma frequency $f_{pe} \approx$ 270 MHz). The stationary probe is located at $\Delta r = 5$ mm and $\Delta z =$ 0 mm. The measurements are taken at a distance of 41 cm from the biased grid.

Fig. 4. High frequency noise, as measured by a capacitive probe, for frequencies around the electron plasma frequency f_{pe} versus position (Dotted line : corresponding potential profile)

a) Grid bias $V_g = 0V$

b) Grid bias $V_g = 20V$

Fig. 5. Radial dependence of the autocorrelation of the high frequency noise for different frequencies. The probe is located 41 cm from the positively biased grid. (V_g = 20V).

Fig. 6. Contours of constant phase (crosses minimum, circles maximum) of the cross power spectral density in the r - z plane ($z \parallel B_0$) at different frequencies. Reference probe tip at Δr = 0 cm, probe shaft along $\Delta r < 0$. The value Δz = 0 corresponds to a distance of 41 cm from the positively biased grid (V_g = 20V).

Fig. 7. Contours of constant phase (crosses minimum, circles maximum) of the cross power spectral density in the r - z plane. ($z \parallel B_0$) at different frequencies. Reference probe tip at Δr = cm, probe shaft along $\Delta r < 0$. The value Δz = 0 corresponds to a distance of 41 cm from the positively biased grid, (V_g = 20V).

Fig. 8. Time position diagram for maxima (circles) and minima (crosses) of the cross power spectral density. The reference probe is at Δz = 0 cm. The wave propagates in the direction of the electron beam (-z direction) with $v_p \approx 1.7.10^8$ cm/sec. The value Δz = 0 corresponds to a distance of 41 cm from the positively biased grid (V_g = 20V).

Fig. 9. Dispersion relation of the high frequency turbulence.

a) Dispersion relation as obtained from correlation measurements (•). The solid line corresponds to the dispersion relation $\omega = kv_b$ ($v_b = 2.1 \cdot 10^8$ cm/sec which corresponds to electron beam energy of 12eV). The square (□) corresponds to the value obtained from the time - position diagram.

b) Electron beam energy versus distance from the biased grid. The dots (o) corresponds to the values obtained from the electron distribution measurements, and (•) the value obtained from the dispersion relation. The line corresponds to the potential difference between the low and high potential side.

Fig.10. Normalized turbulent wave energy W/nT_e for frequencies below the ion plasma frequency as a function of position for V_g = 20V.

Fig.11. Power spectra (linear scale) for different values of the normalized turbulent wave energy W/nT_e, as measured by capacitive probe. The two spectra at the top are those measured on the high potential side of the jump. The other spectra were measured on the low potential side.

Fig.12. Phase contours of the cross power spectral density in the r - z plane for different frequencies ($W/nT_e = 3.6 \times 10^{-3}$, f_{pi} = 1,23 MHz). The electron drift is in the negative z direction. Thick lines (━) correspond to the maximua, thin lines (—) to the minimua. The measured points are omitted for clarity. The reference probe tip is at $\Delta r = 0$, probe shaft along $\Delta r < 0$. The value $\Delta z = 0$ corresponds to a distance of 185 cm from the positively biased grid (V_g = 20V).

Fig.13. Phase contours of the cross power spectral density in the r - z plane for different frequencies ($W/nT_e = 3,6 \times 10^{-3}$, f_{pi} = 1.23MHz). The electron drift is in the negative z direction. The lines correspond to the position of the maxima. The measured points as the position of the minima are omitted for clarity. The reference probe tip is at $\Delta r = 0$, probe shaft along $\Delta r < 0$. The value $\Delta z = 0$ corresponds to a distance of 185 cm form the positively biased grid (V_g = 20V).

Fig.14. Phase contours of the cross power spectral density in the r - z plane for different frequencies ($W/nT_e = 1.25 \times 10^{-2}$, f_{pi} = 1.11 MHz). The electron drift is in the negative z direction. Thick lines (━) correspond to the maxima, thin lines (—) to the minima. The measured points are omitted for clarity. The reference probe tip is at $\Delta r = 0$, probe shaft along $\Delta r < 0$. The value $\Delta z = 0$ corresponds to a distance of 113 cm from the positively biased grid (V_g = 20V).

Fig.15. Phase contours of the cross power spectral density in the r - z plane for different frequencies.(W/nT_e = 1,25 x 10^{-3}, f_{pi} = 1,11MHz). The electron drift is in the negative z direction. Lines correspond to the the postion of the maximua. The measured points as well as the position of the minima are omitted for clarity. The reference probe tip is at $\Delta r = 0$, probe shaft along $\Delta r < 0$. The value $\Delta z = 0$ corresponds to a distance of 113 cm from the positively biased grid (V_g = 20V).

Fig.16. Phase contours of the cross power spectral density in the r - z for plane for different frequencies. (W/nT_e= 6,25 x 10^{-2}, f_{pi} = 0.90MHz). The electron drift is in the négative z direction. Thick (▬) and thin (—) lines correspond to maxima and minima respectively. The measured points are omitted for clarity. The reference probe tip is at $\Delta r = 0$, probe shaft along $\Delta r < 0$. The value $\Delta z = 0$ corresponds to a distance of 77 cm from the positively biased grid .

Fig.17. Phase contours of the cross power spectral density in the r - z plane for different frequencies (W/nT_e = 6,25 x 10^{-2}, f_{pi} = 0.90 MHz). The electron drift is in the negative z direction. Lines correspond to the position of the minima. Maxima positions have been omitted for clarity. The reference probe tip is at $\Delta r = 0$, probe shaft along $\Delta r < 0$. The value $\Delta z = 0$ corresponds to a distance of 77 cm from the positively biased grid.

Fig.18. Cone angle (θ = arctan $k_{\parallel}/k_{\perp}$) versus frequency for three different values of low frequency fluctuation level W/nT_e. The corresponding distances from the polarized grid are z = 185 cm, z = 113 cm and z = 77 cm, respectively.

Fig.19. Phase contours of the cross power spectral density in a normal section of the device (x-y plane, $\perp B_0$). ($W/nT_e = 3.6 \times 10^{-3}$, f_{pi} = 1.23MHz). The reference probe tip is at $\Delta y = 0$, probe shaft along $\Delta y < 0$. The position (Δx, Δy) = (0,0) correspond to the axis of the device.

Fig.20. Radial time-position diagram for maxima (closed circles) and minima (open circles) of the cross power spectral density at 200kHz. The reference probe is on the axis of the device. The distance from the polarized grid is indicated by z. The waves propagates radially in the negative Δr direction.

Fig.21. Radial time-position diagram for maxima (closed circles) and minima (open circles) of the cross power spectral density at 400 kHz. The reference probe is on the axis of the device. The distance from the polarized grid is indicated by z. The waves The waves propagates radially in both directions ($\pm \Delta r$) separated by a region of standing waves.

Fig.22. Graph of $k_{\perp}$ versus $k_{\parallel}$ for different values of W/nT_e as obtained from the correlation measurement.

Fig.23. Measured dispersion relation (•) of the unstable waves for three different values of W/nT_e :

a) $W/nT_e = 3,6 \times 10^{-3}$; b) $W/nT_e = 1,25 \times 10^{-2}$; and

c) $W/nT_e = 6,25 \times 10^{-2}$.

The solid line is the theoretical dispersion relation of the ion acoustic mode. The temperature ratio T_e/Ti used for the calculation is the experimental value obtained from probe measurements.

Fig.24. Radial behavior of the autocorrelation of the low frequency fluctuations for different frequencies at a distance of 77 cm from the polarized grid.

Fig.25. Spectral density I(k) at a distance of 77 cm from the biased grid. ($W/nT_e = 6.25 \times 10^{-2}$).

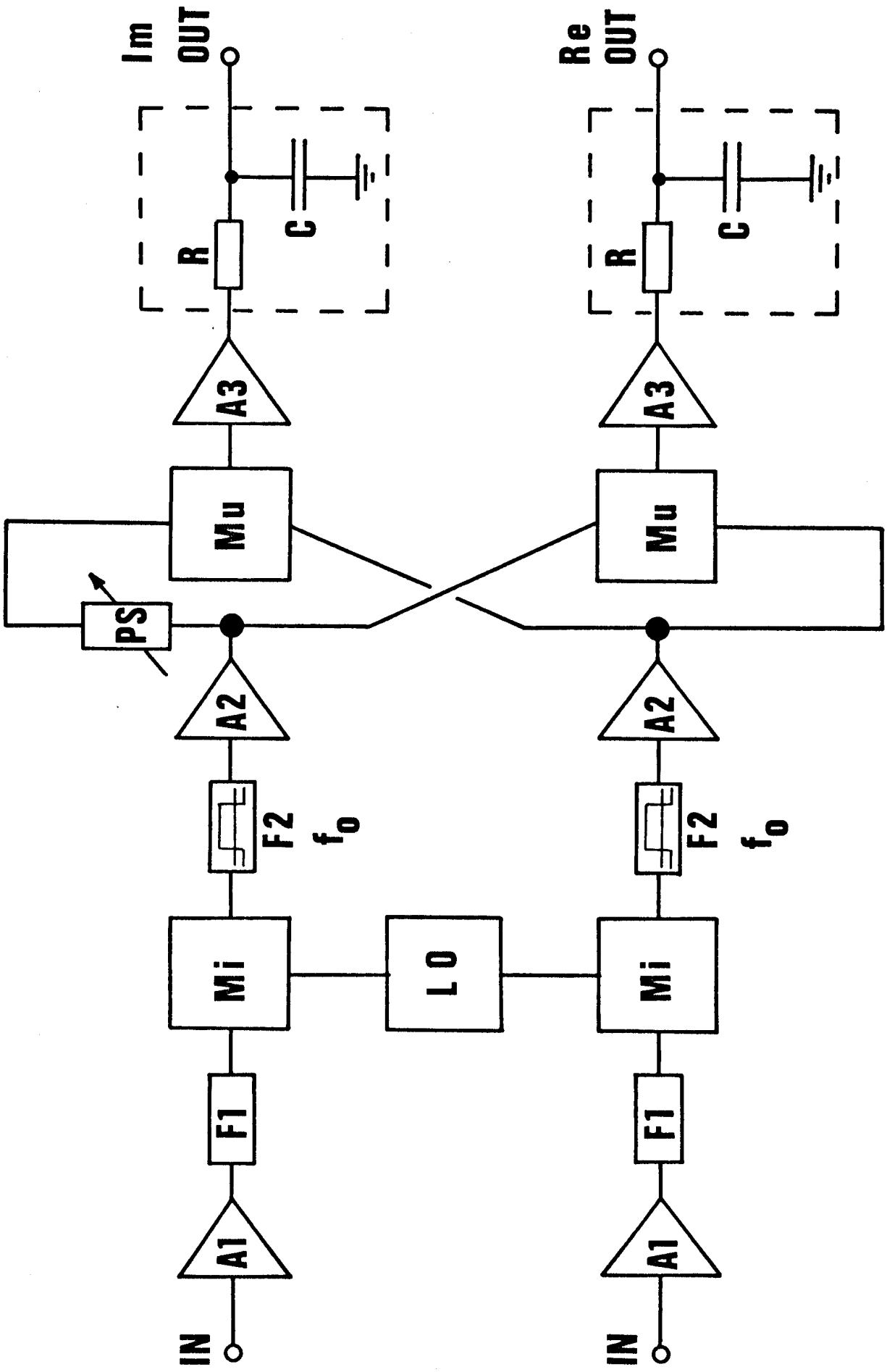
Im OUT
Re OUT
R
C
R
C
A3
A3
Mu
Mu
PS
A2
A2
F2
f_o
F2
f_o
Mi
LO
Mi
F1
F1
A1
A1
IN
IN

fig. 1

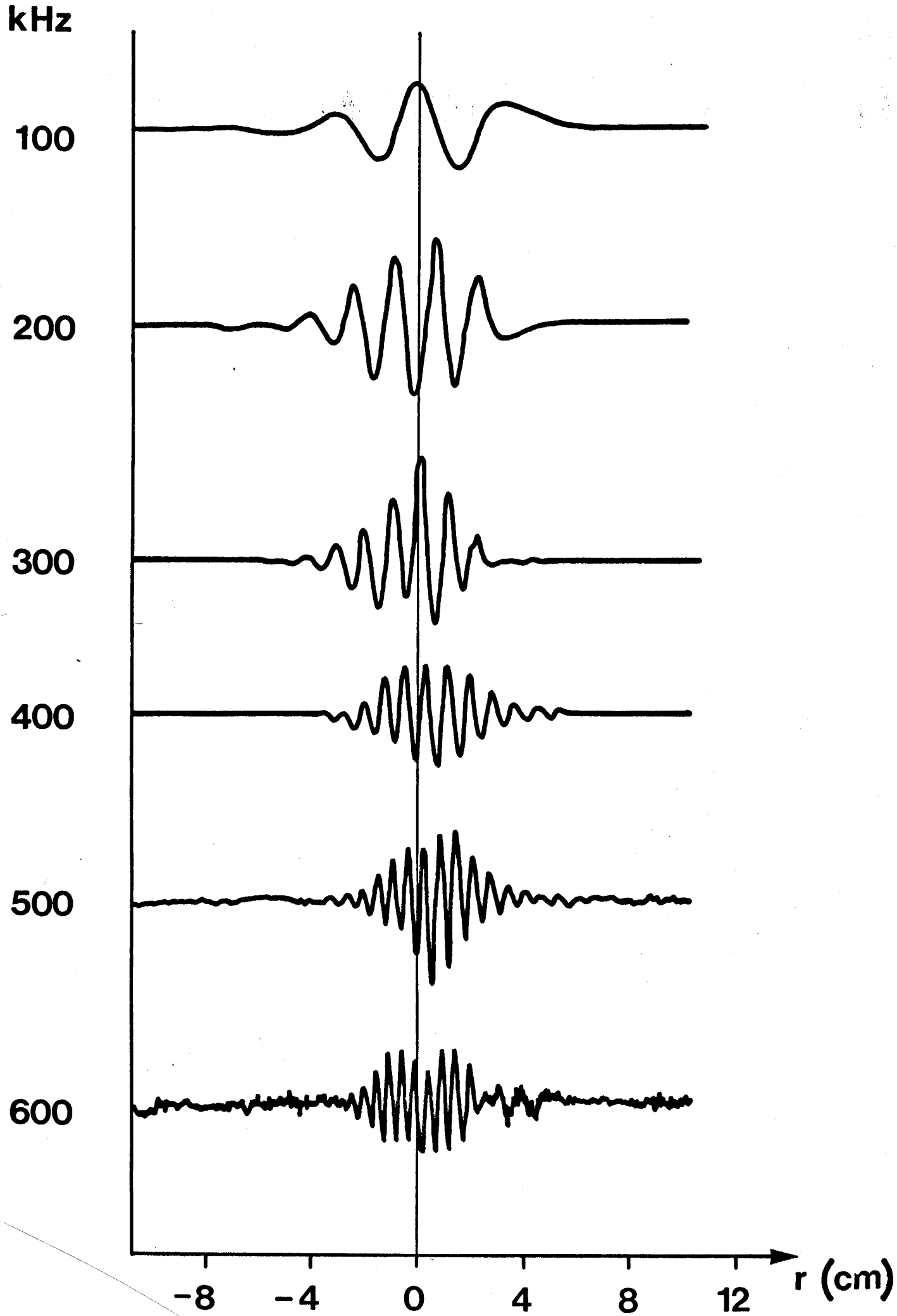

fig. 2

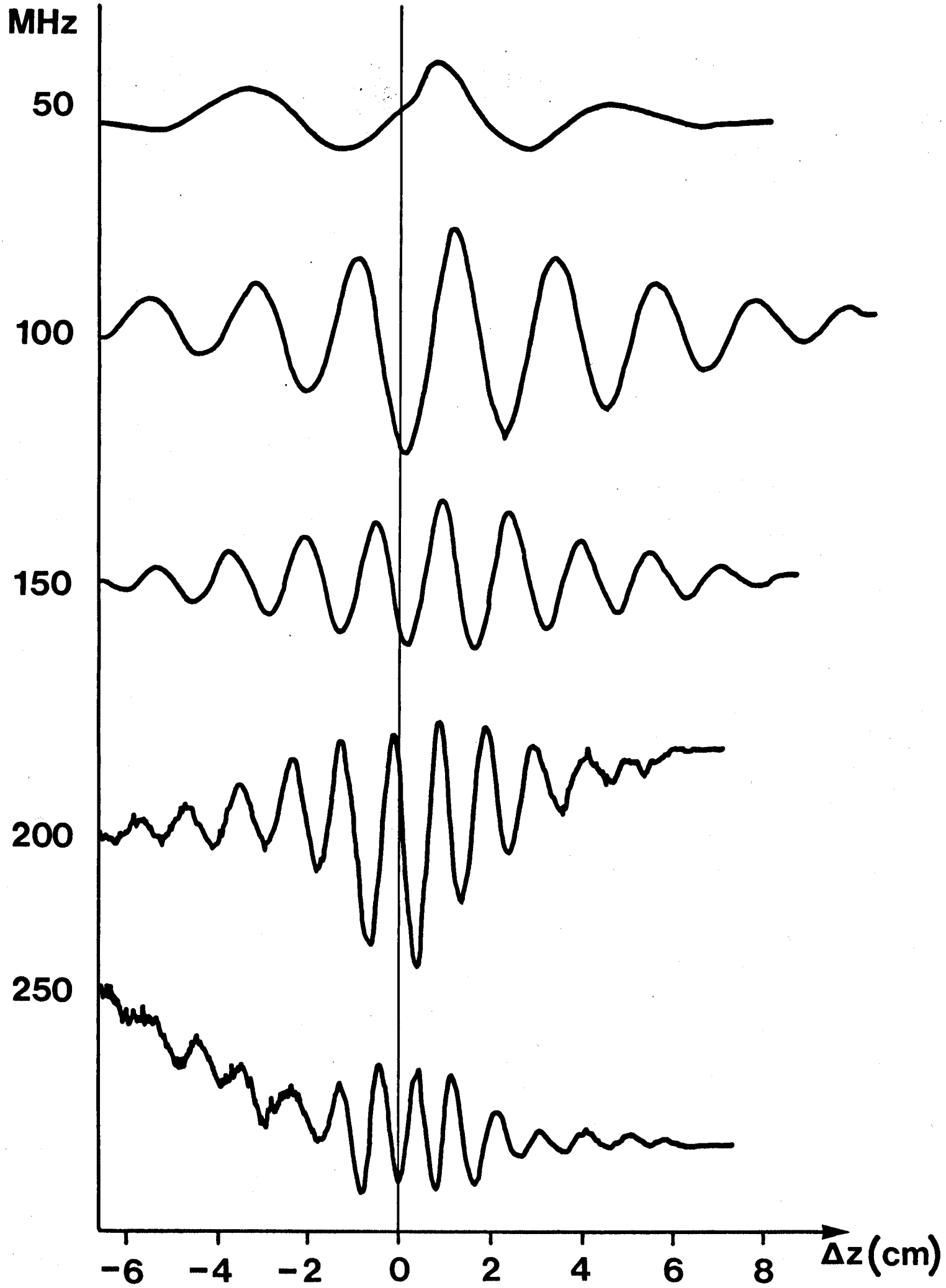

fig. 3

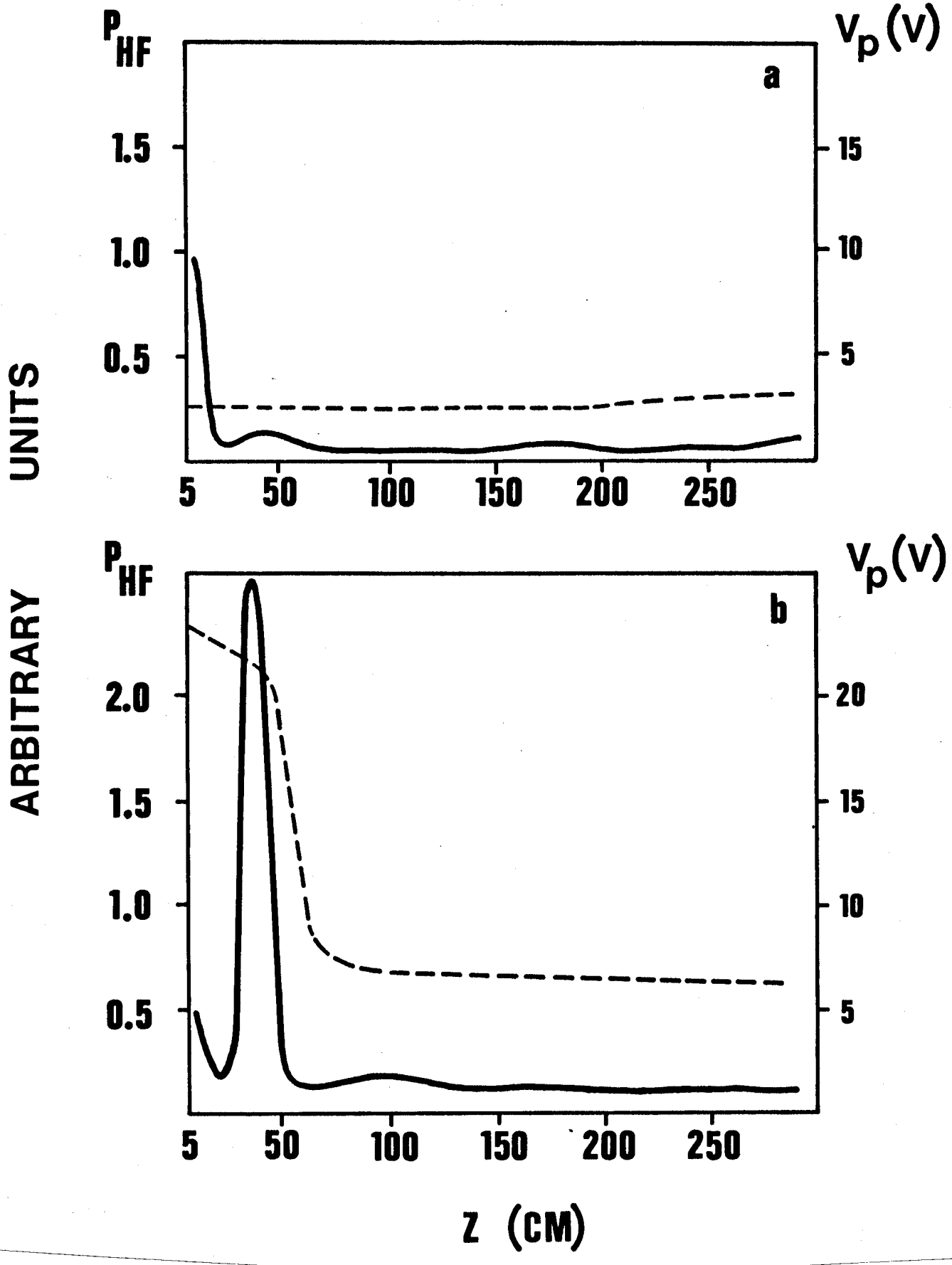
P HF
V p (V)
a
1.5
1.0
0.5
15
10
5
UNITS
5
50
100
150
200
250
P HF
V p (V)
b
2.0
1.5
1.0
0.5
20
15
10
5
ARBITRARY
5
50
100
150
200
250
Z (CM)

fig. 4

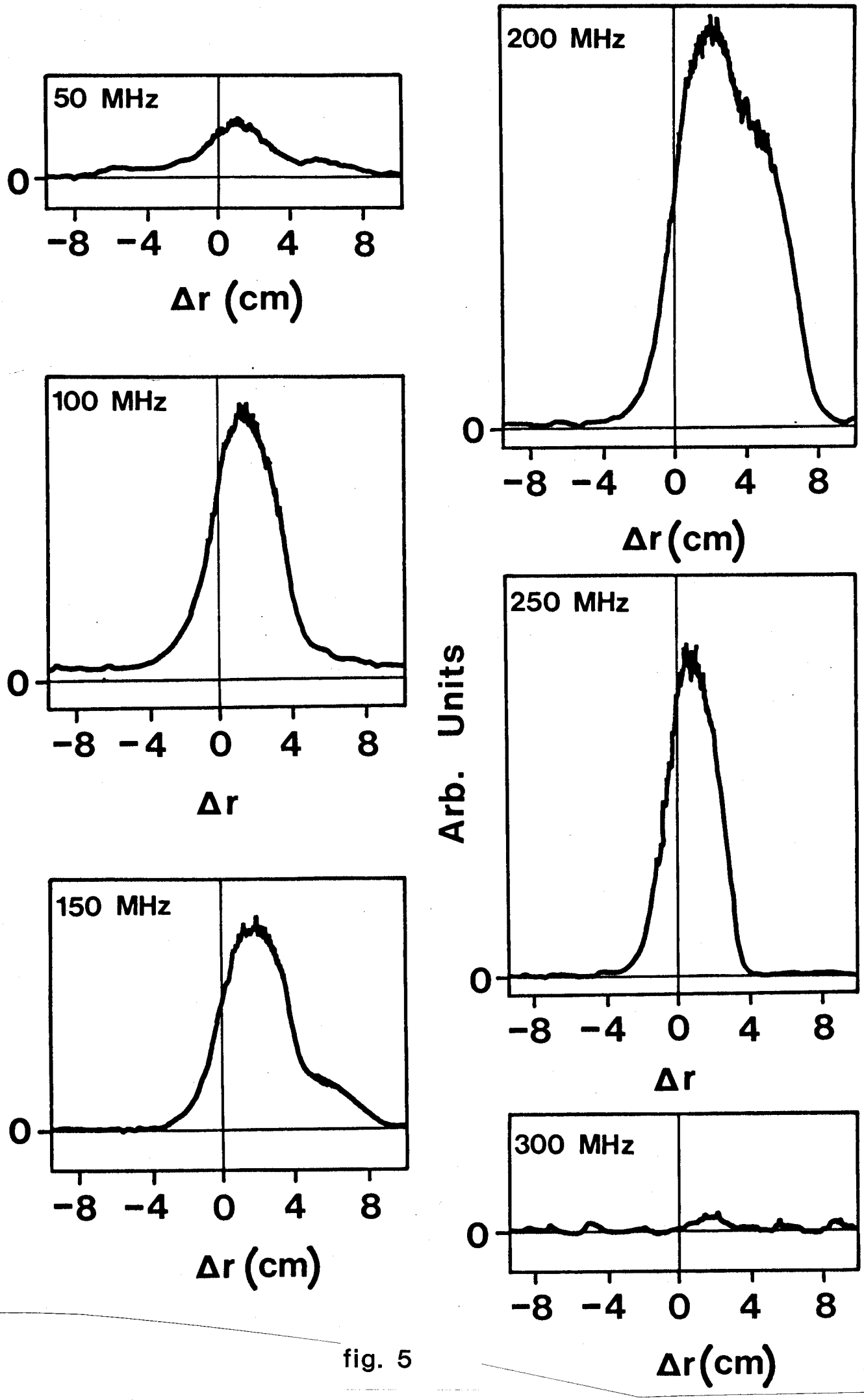
50 MHz
0
-8 -4 0 4 8
Δr (cm)
100 MHz
0
-8 -4 0 4 8
Δr
150 MHz
0
-8 -4 0 4 8
Δr (cm)
200 MHz
0
-8 -4 0 4 8
Δr (cm)
250 MHz
Arb. Units
0
-8 -4 0 4 8
Δr
300 MHz
0
-8 -4 0 4 8
Δr (cm)

fig. 5

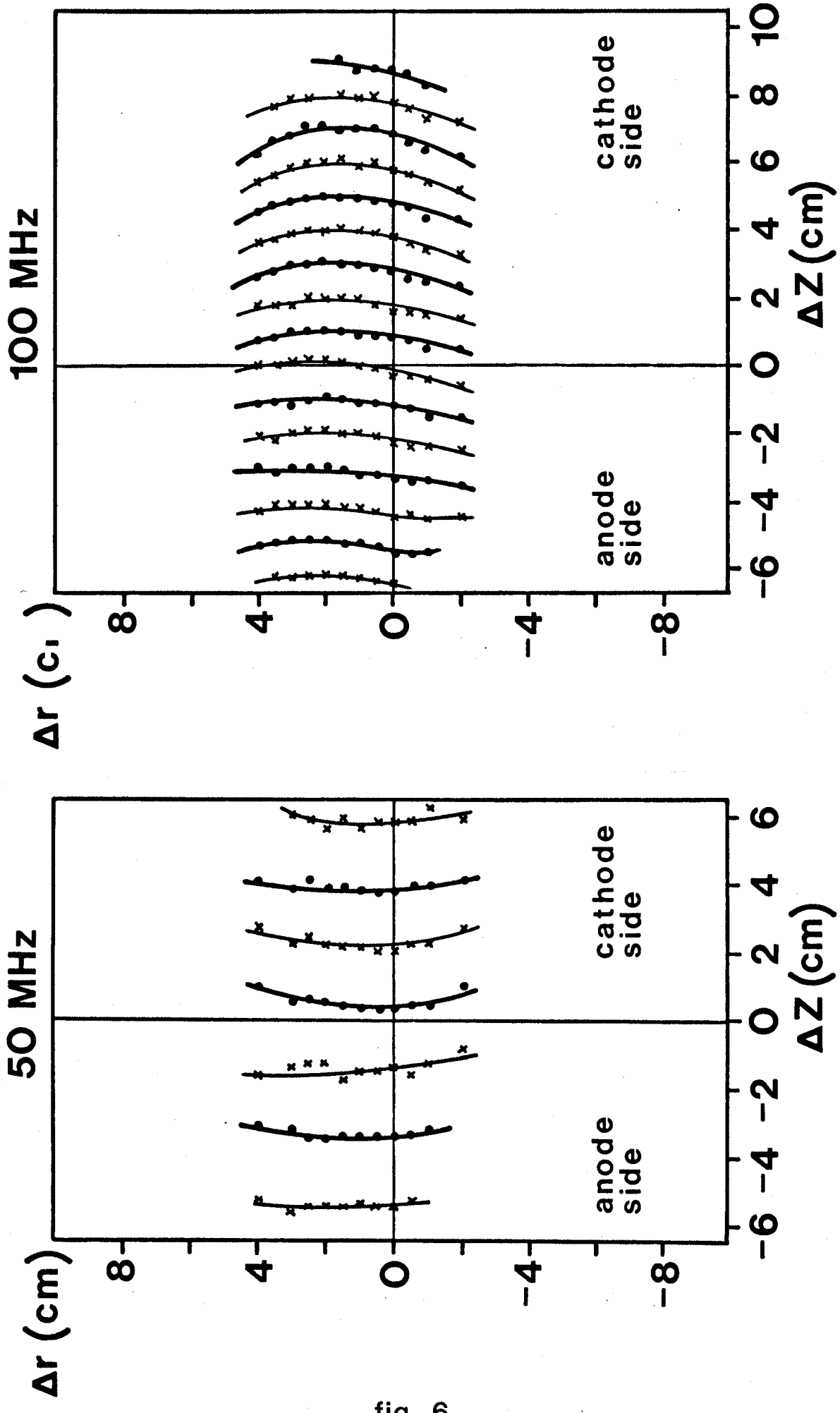
100 MHz
Δr (cm)
8
4
0
-4
-8
cathode side
anode side
-6 -4 -2 0 2 4 6 8 10
ΔZ (cm)
50 MHz
Δr (cm)
8
4
0
-4
-8
cathode side
anode side
-6 -4 -2 0 2 4 6
ΔZ (cm)

fig. 6

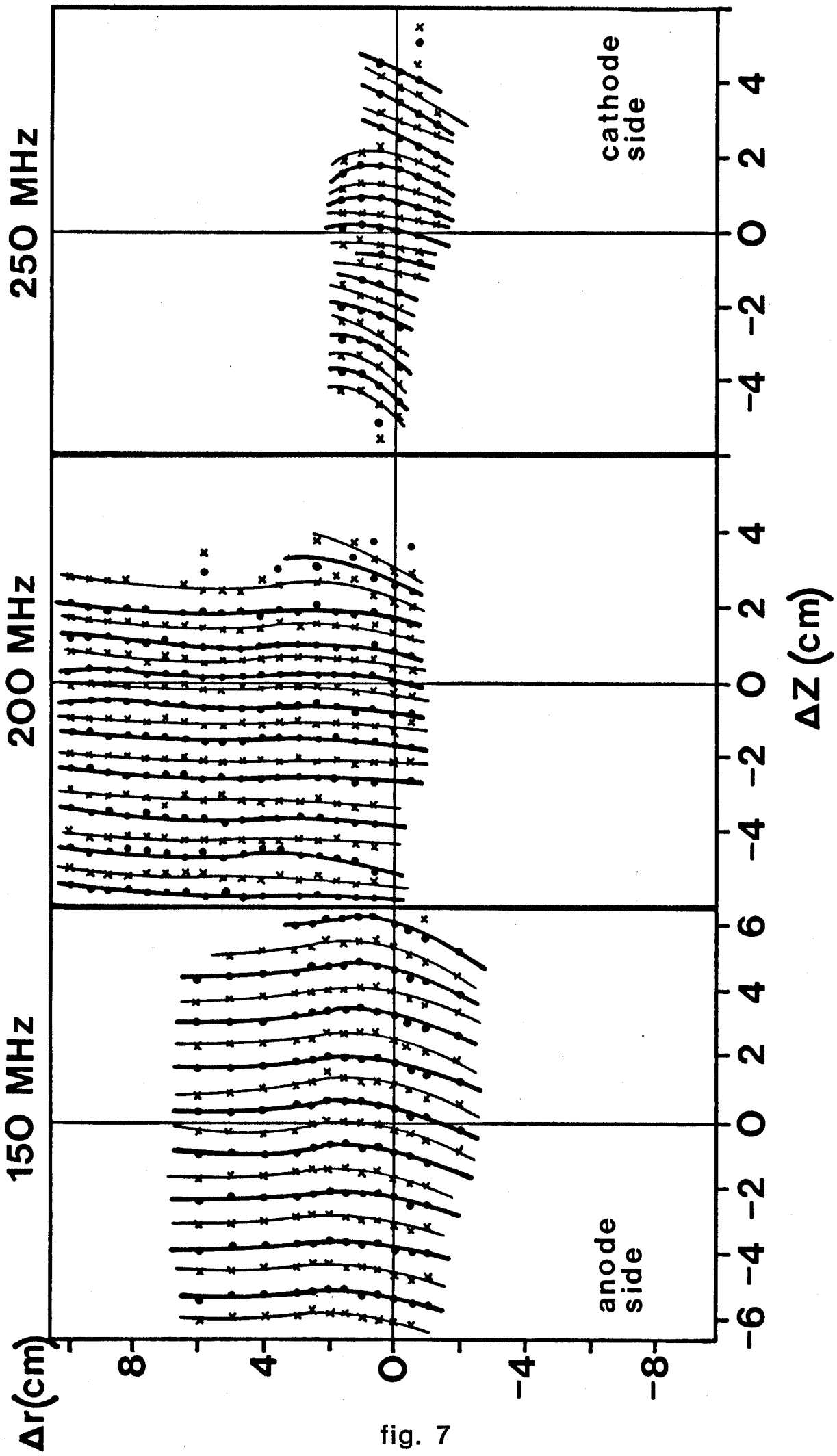
250 MHz
200 MHz
150 MHz
cathode side
anode side
Δr(cm)
ΔZ (cm)
8
4
0
-4
-8
-6 -4 -2 0 2 4 6

fig. 7

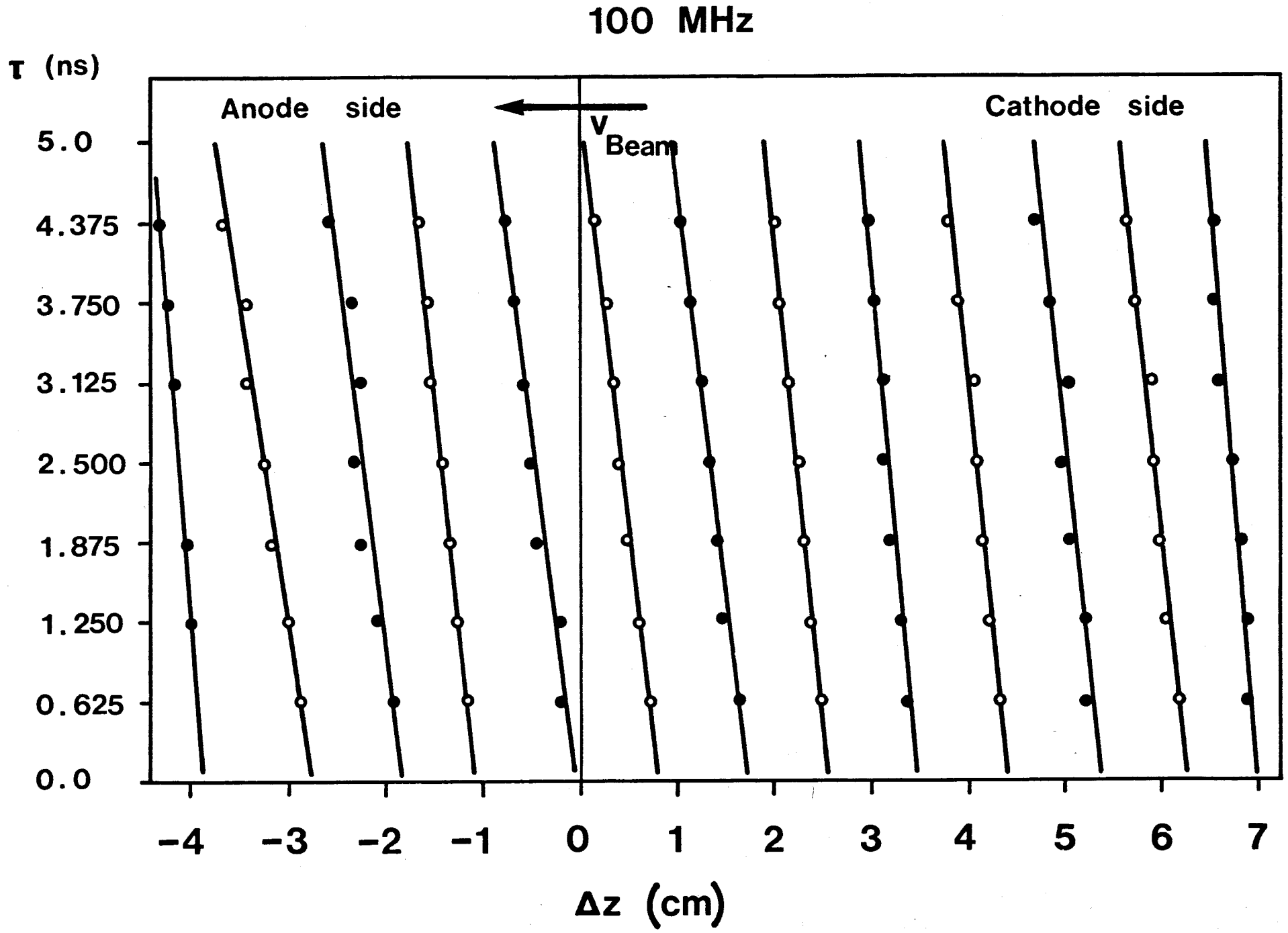
100 MHz
τ (ns)
Anode side
Cathode side
v_{Beam}
5.0
4.375
3.750
3.125
2.500
1.875
1.250
0.625
0.0
−4
−3
−2
−1
0
1
2
3
4
5
6
7
Δz (cm)

fig. 8

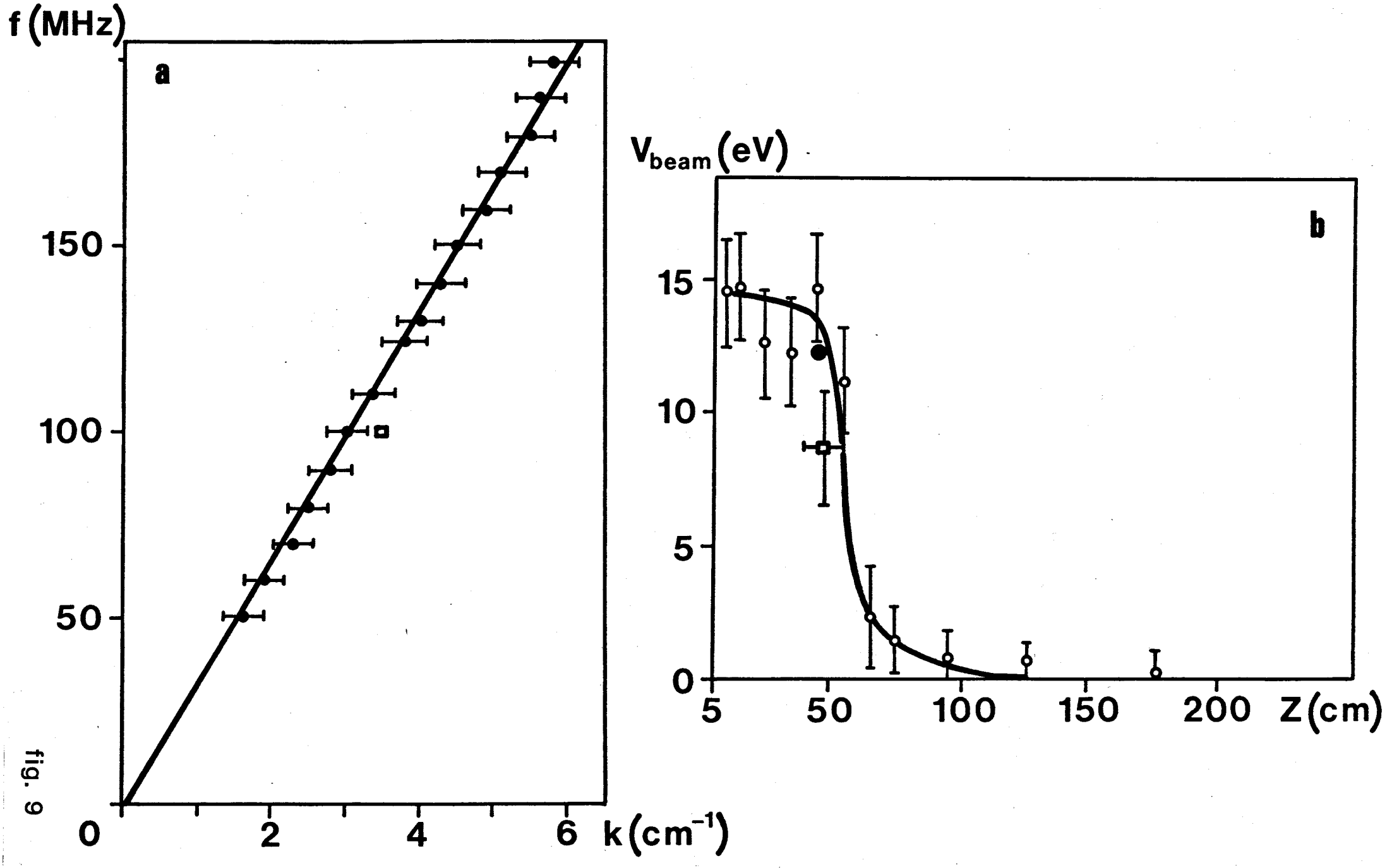
f (MHz)
a
150
100
50
0
2
4
6
k (cm⁻¹)
V beam (eV)
b
15
10
5
0
5
50
100
150
200
Z (cm)

fig. 9

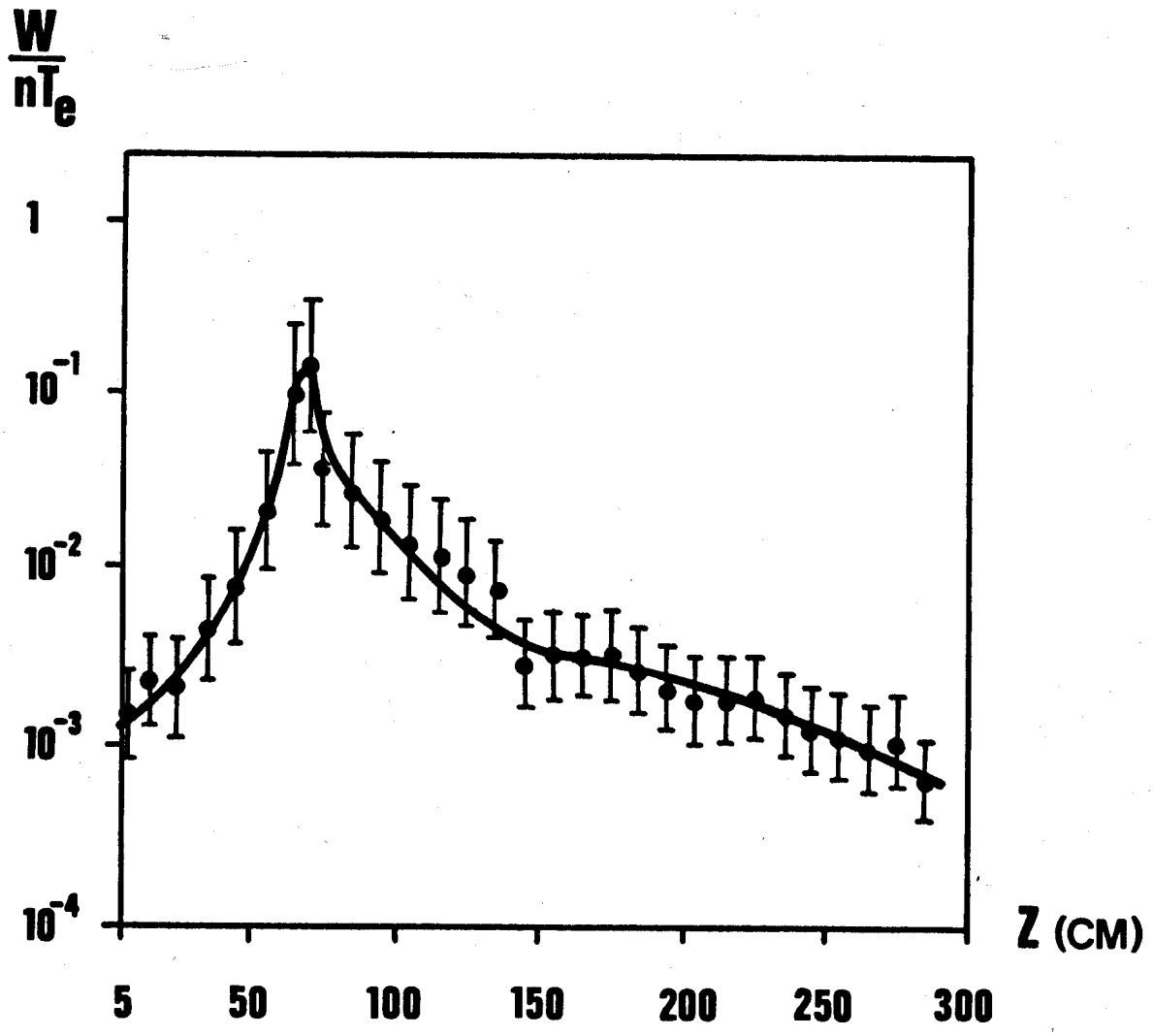

fig. 10

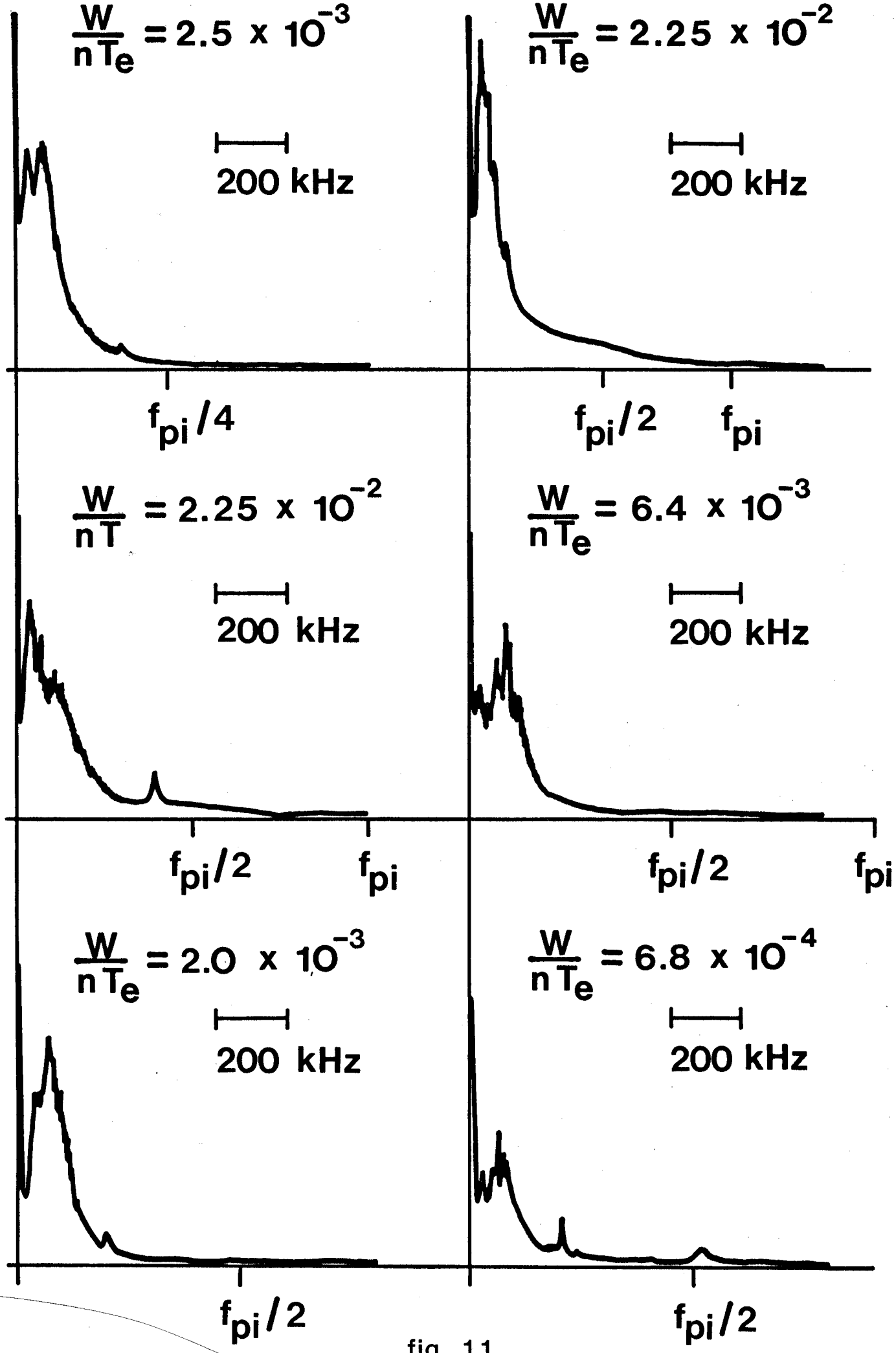
$\frac{W}{nT_e} = 2.5 \times 10^{-3}$
200 kHz
$f_{pi}/4$
$\frac{W}{nT_e} = 2.25 \times 10^{-2}$
200 kHz
$f_{pi}/2$
f_{pi}
$\frac{W}{nT} = 2.25 \times 10^{-2}$
200 kHz
$f_{pi}/2$
f_{pi}
$\frac{W}{nT_e} = 6.4 \times 10^{-3}$
200 kHz
$f_{pi}/2$
f_{pi}
$\frac{W}{nT_e} = 2.0 \times 10^{-3}$
200 kHz
$f_{pi}/2$
$\frac{W}{nT_e} = 6.8 \times 10^{-4}$
200 kHz
$f_{pi}/2$

fig. 11

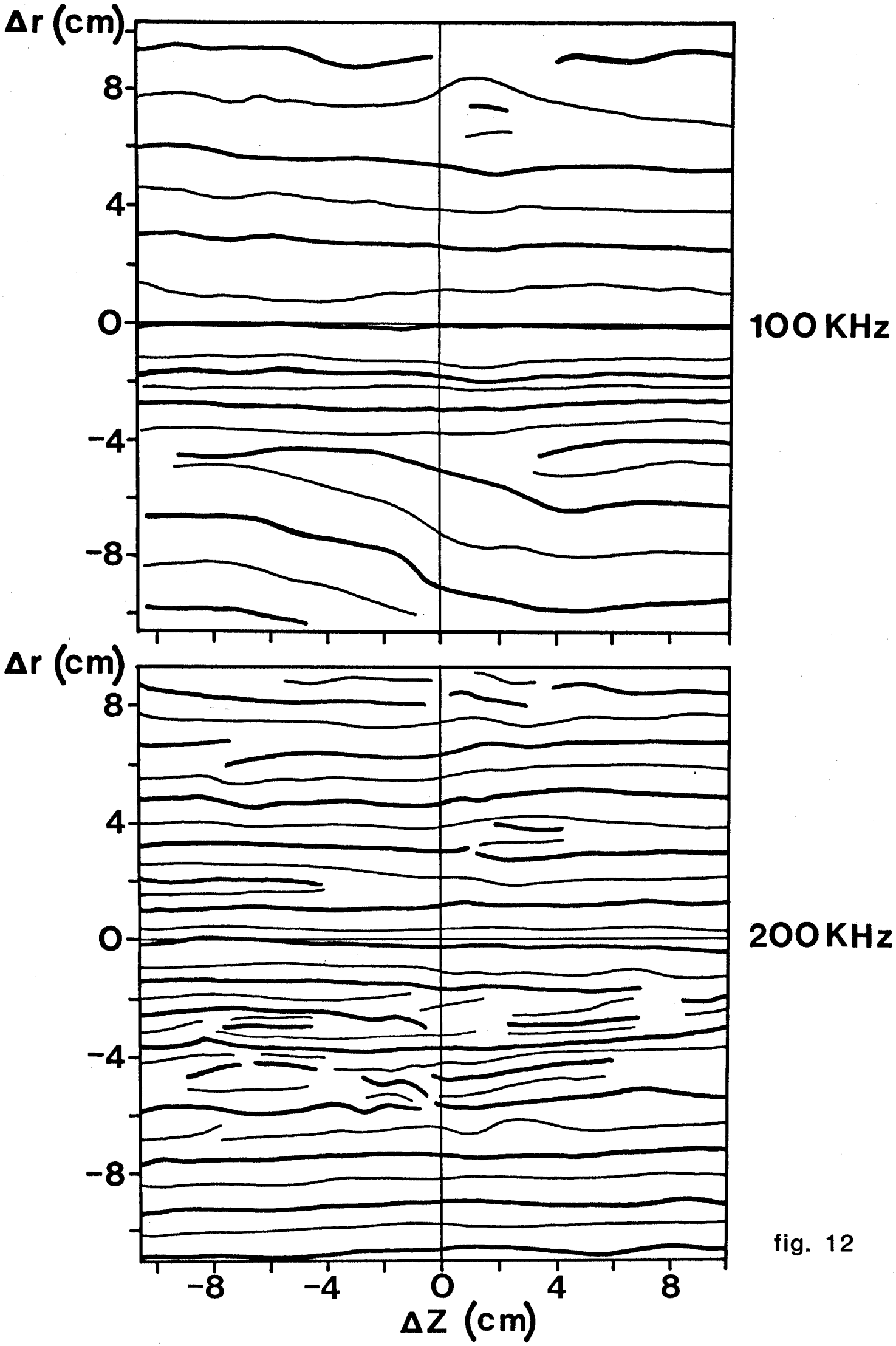

fig. 12

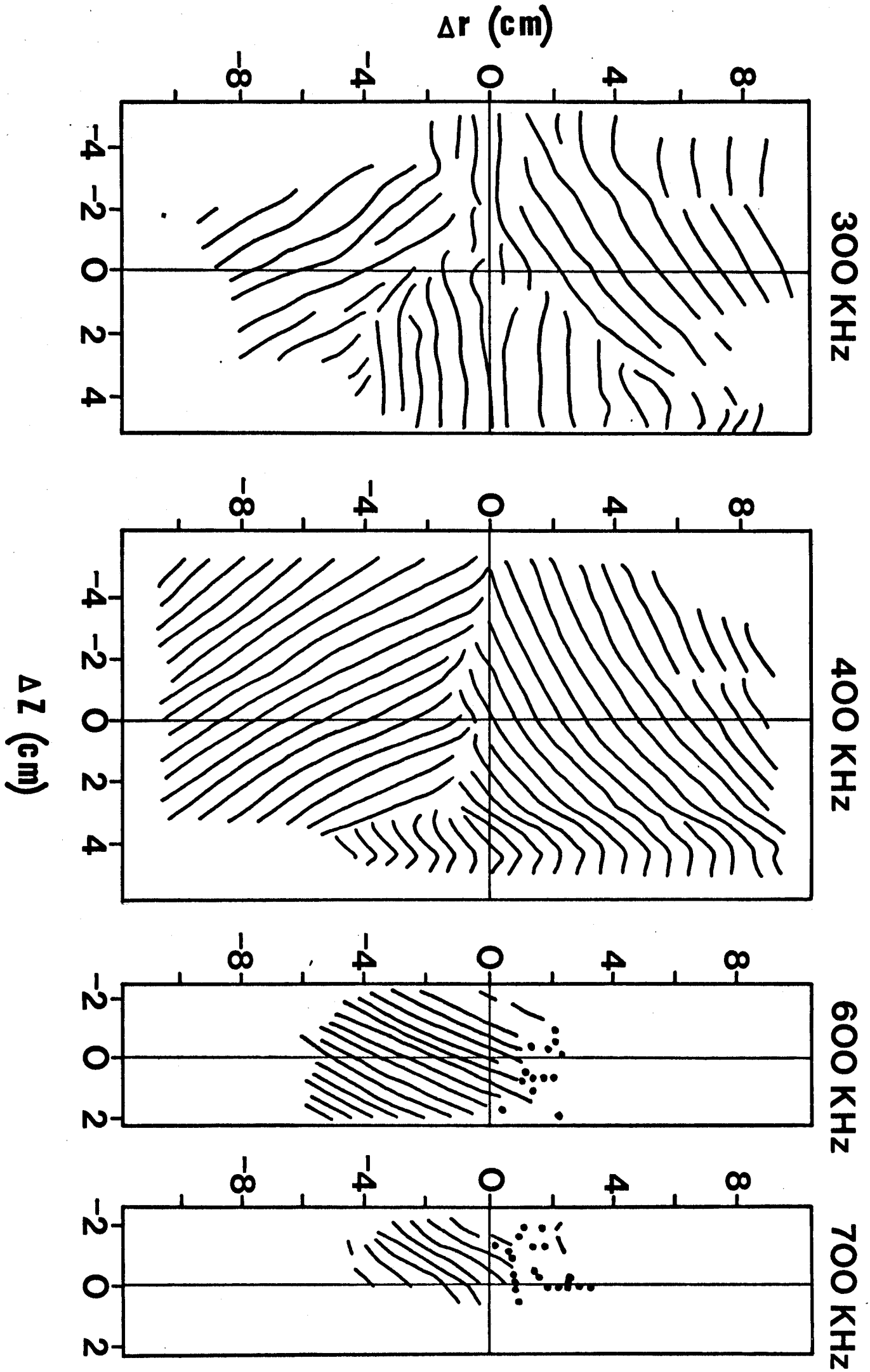

fig. 13

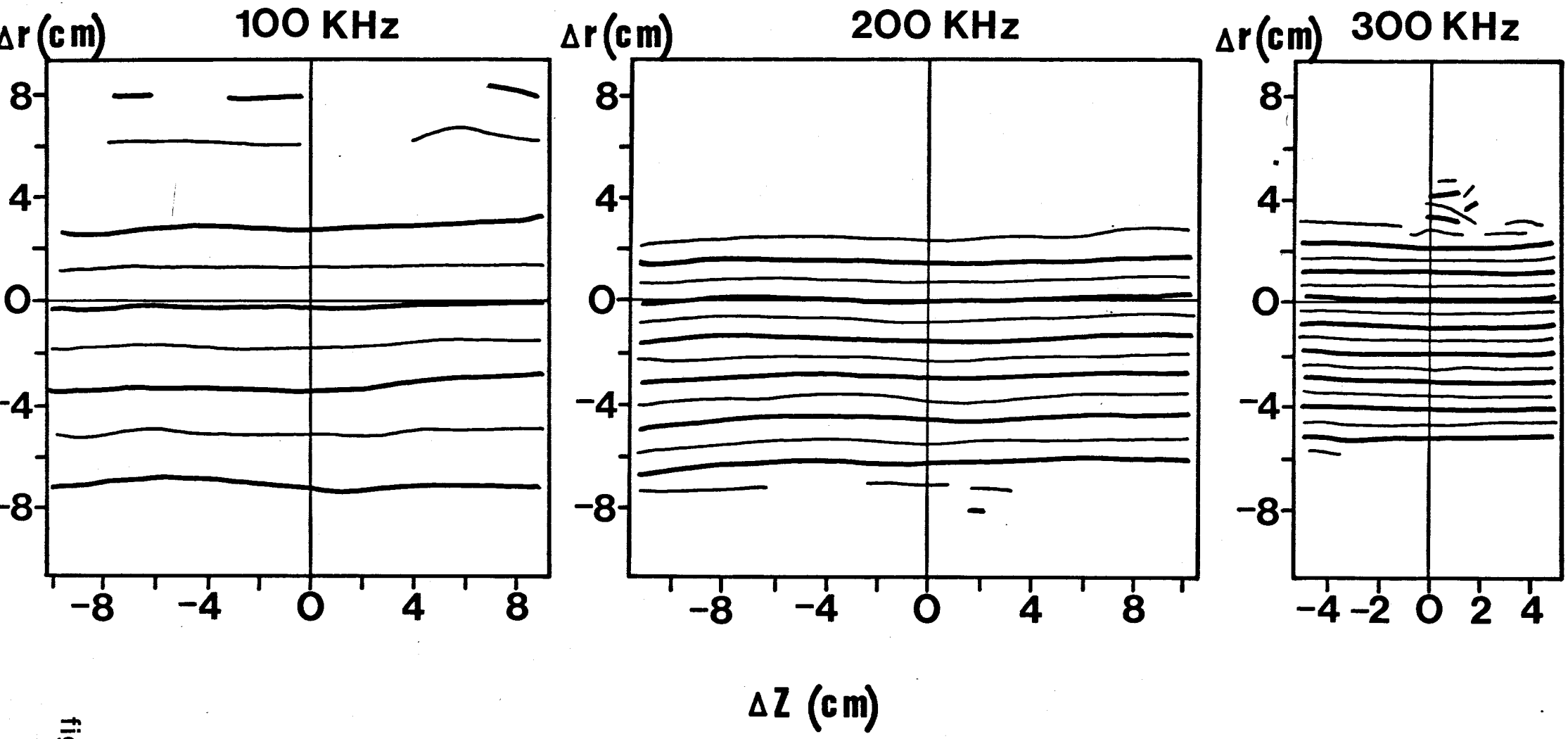
Δr (cm)
100 KHz
Δr (cm)
200 KHz
Δr (cm)
300 KHz
8
4
0
-4
-8
-8 -4 0 4 8
-8 -4 0 4 8
-4 -2 0 2 4
ΔZ (cm)

fig. 14

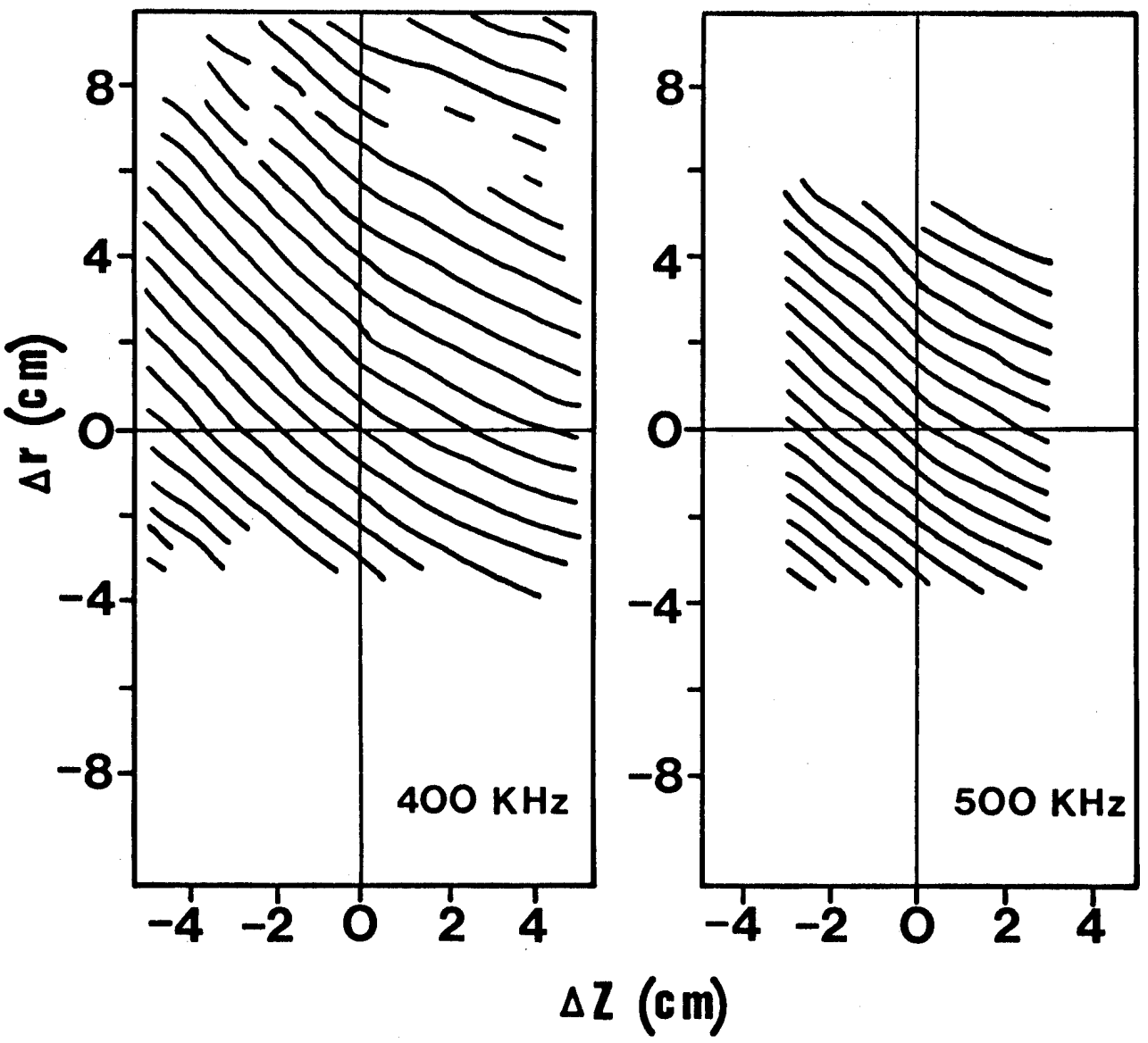
8
4
0
-4
-8
Δr (cm)
400 KHz
500 KHz
-4 -2 0 2 4
ΔZ (cm)

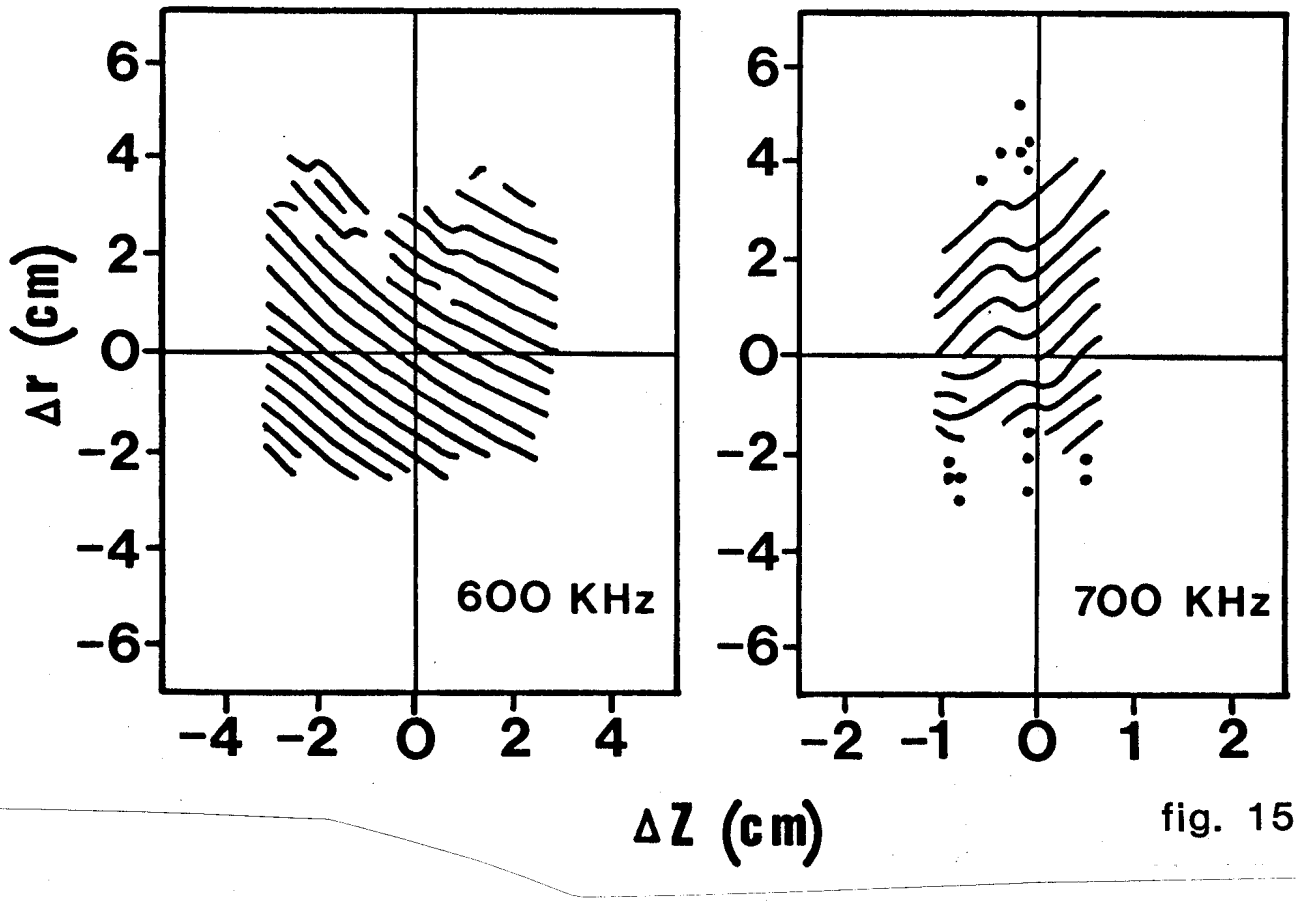
6
4
2
0
-2
-4
-6
Δr (cm)
600 KHz
700 KHz
-4 -2 0 2 4
-2 -1 0 1 2
ΔZ (cm)

fig. 15

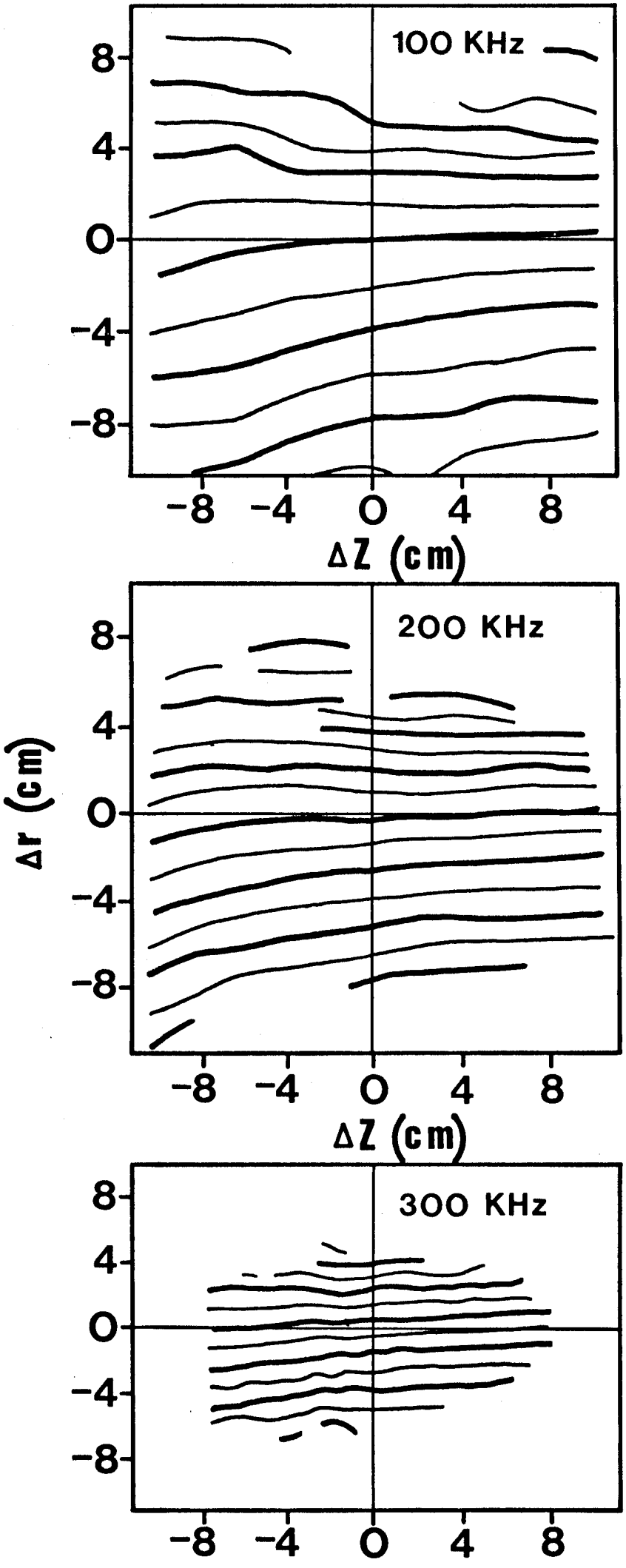

fig. 16

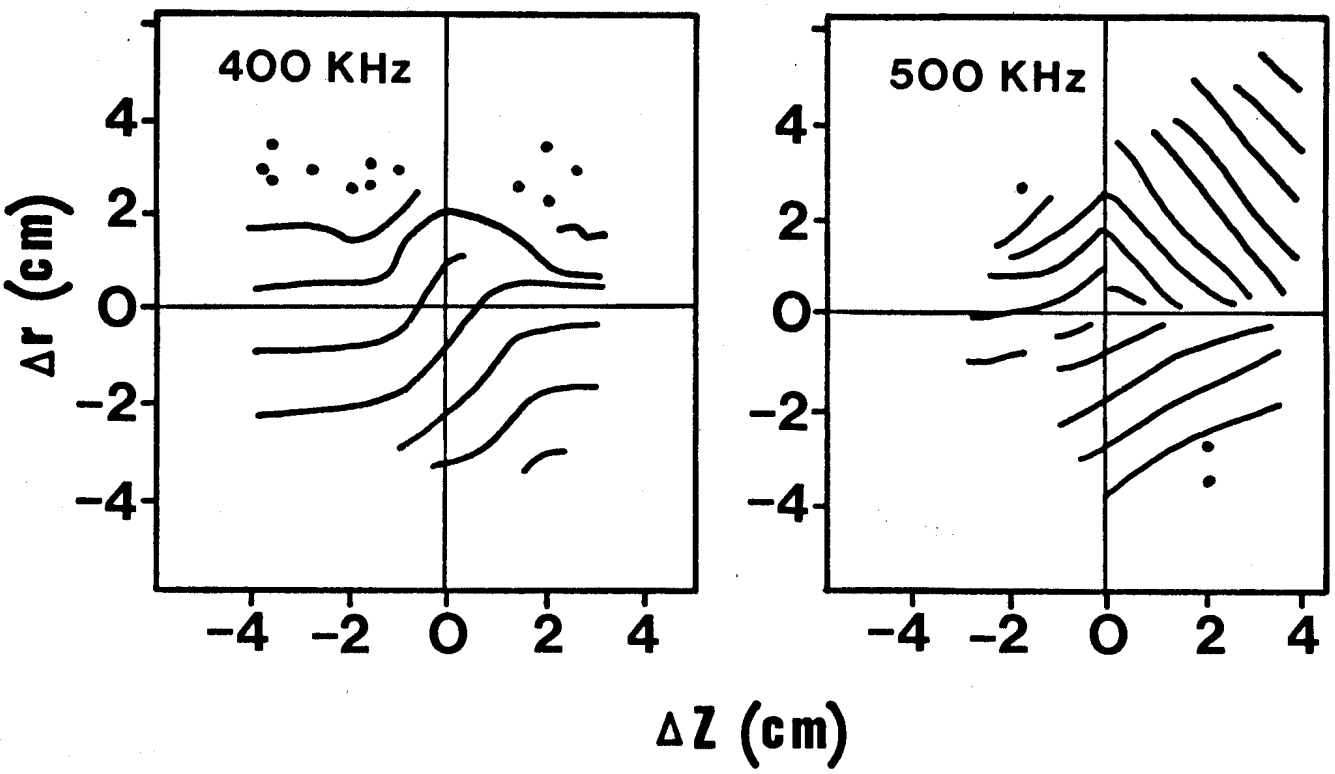
400 KHz
500 KHz
Δr (cm)
4
2
0
-2
-4
-4 -2 0 2 4
ΔZ (cm)

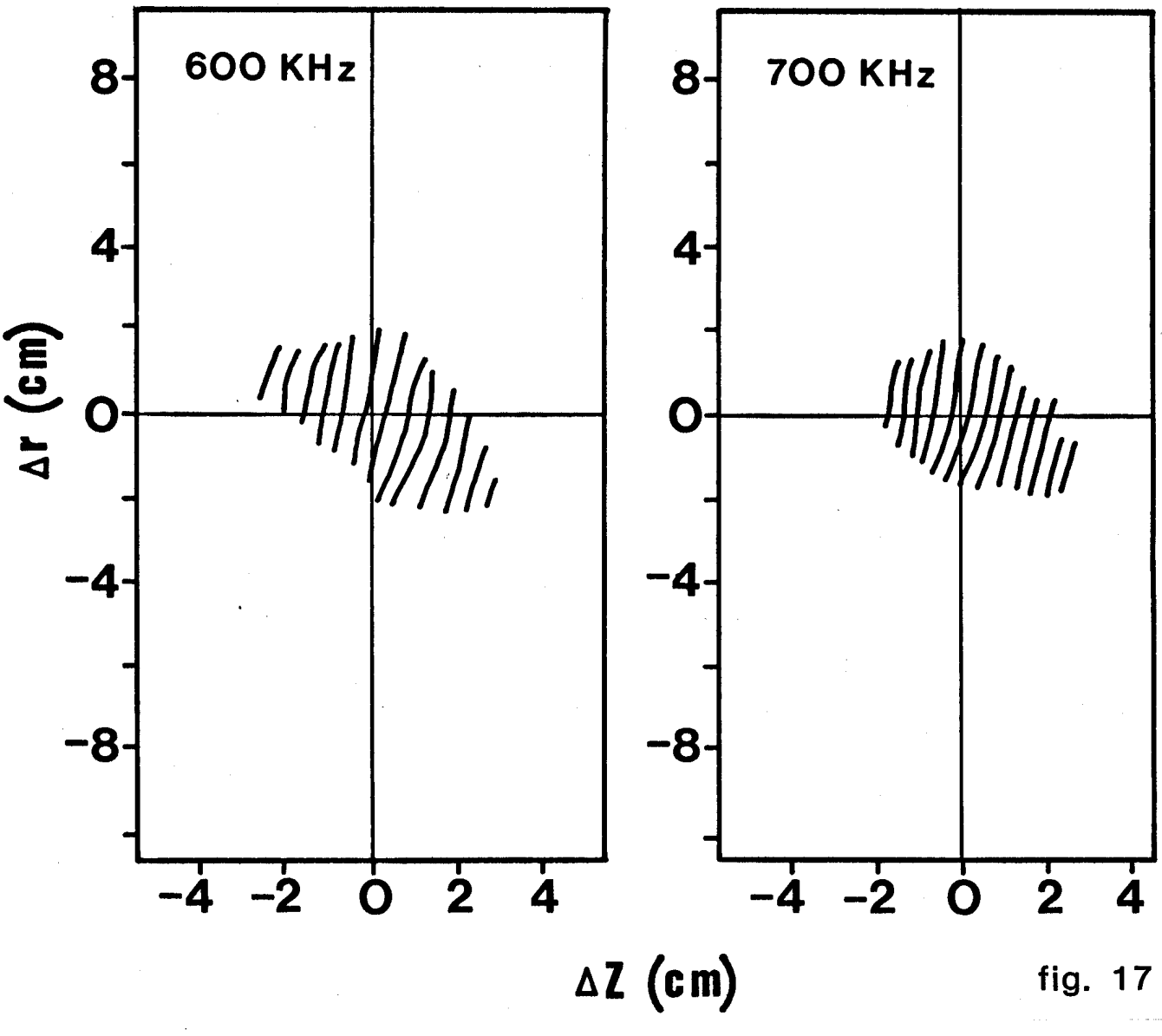
600 KHz
700 KHz
Δr (cm)
8
4
0
-4
-8
-4 -2 0 2 4
ΔZ (cm)

fig. 17

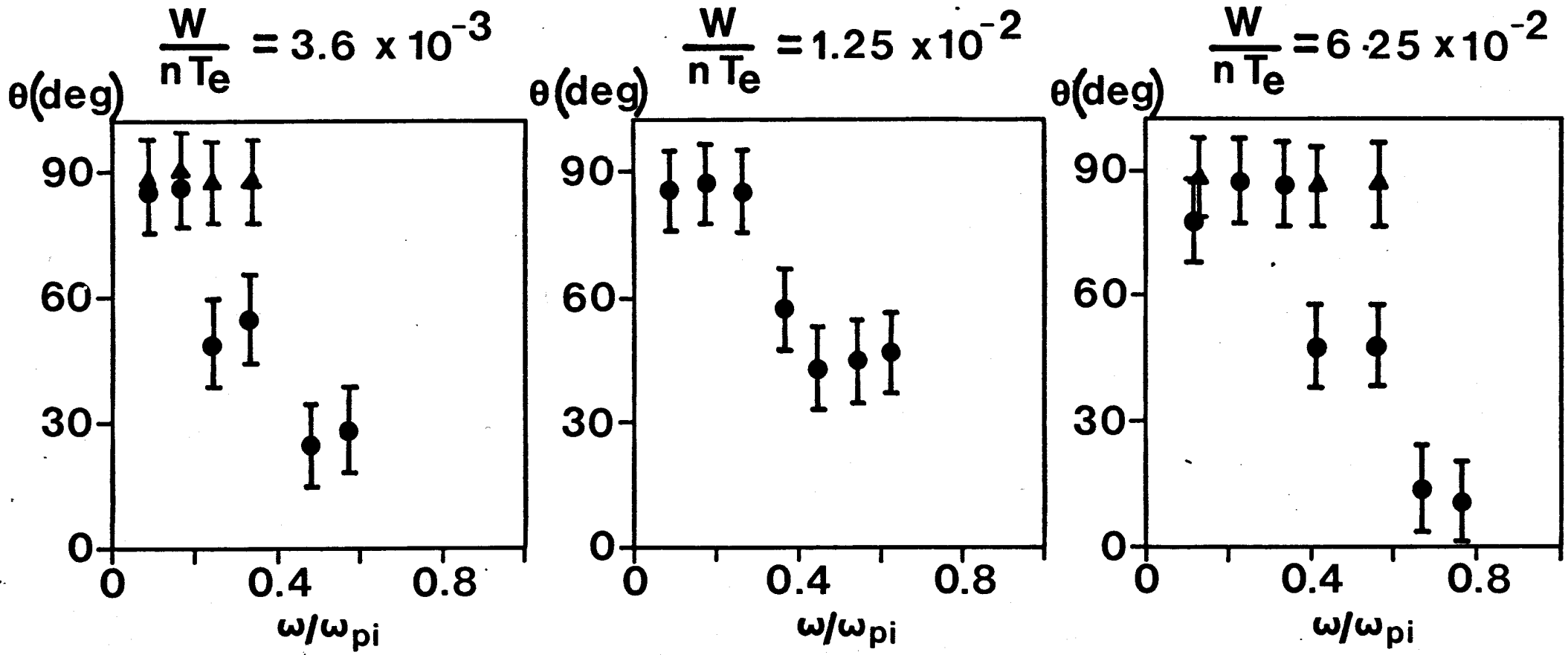
$\frac{W}{n T_e} = 3.6 \times 10^{-3}$
$\frac{W}{n T_e} = 1.25 \times 10^{-2}$
$\frac{W}{n T_e} = 6.25 \times 10^{-2}$
θ(deg)
90
60
30
0
0
0.4
0.8
ω/ω_{pi}

fig. 18

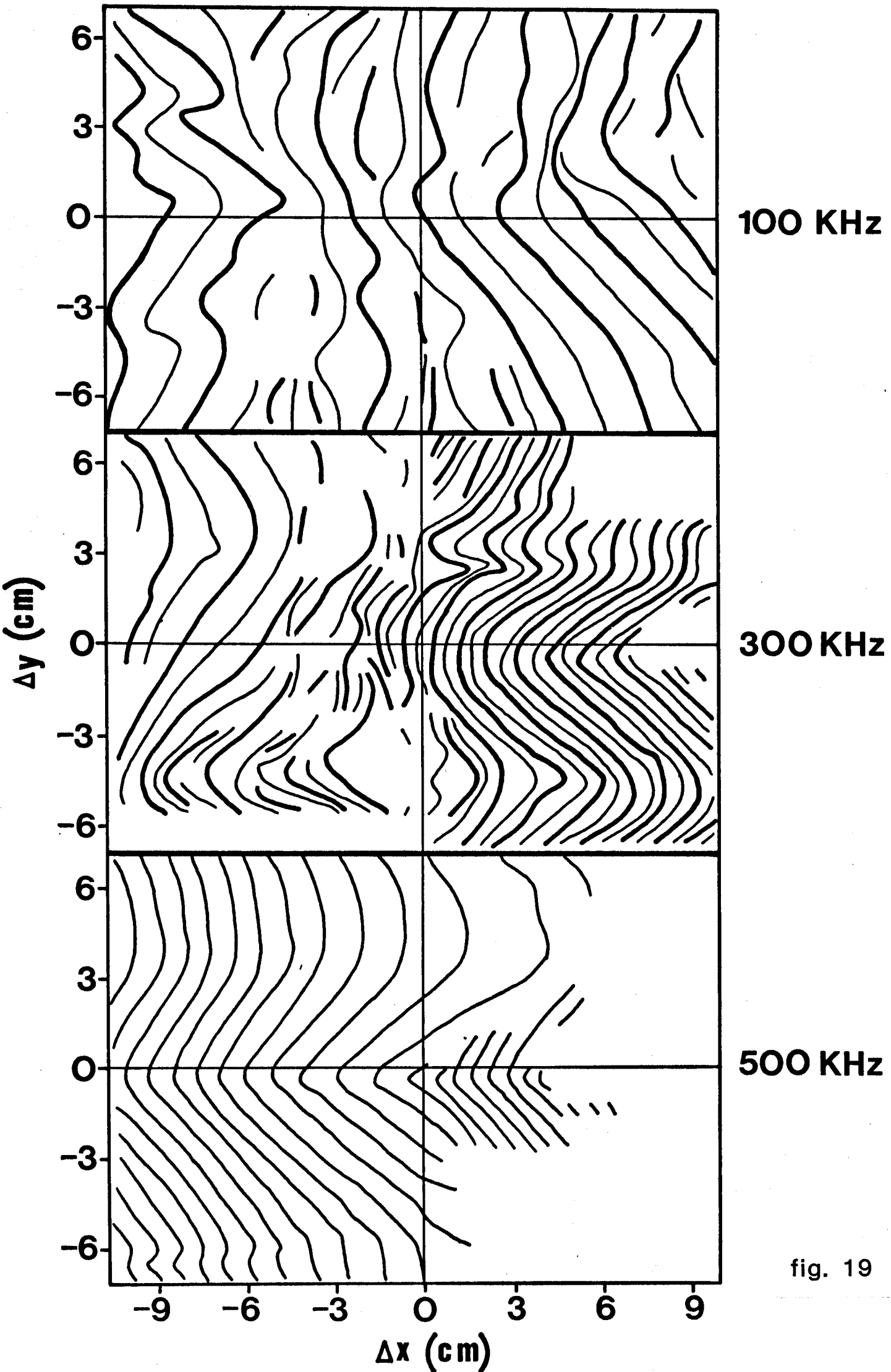

fig. 19

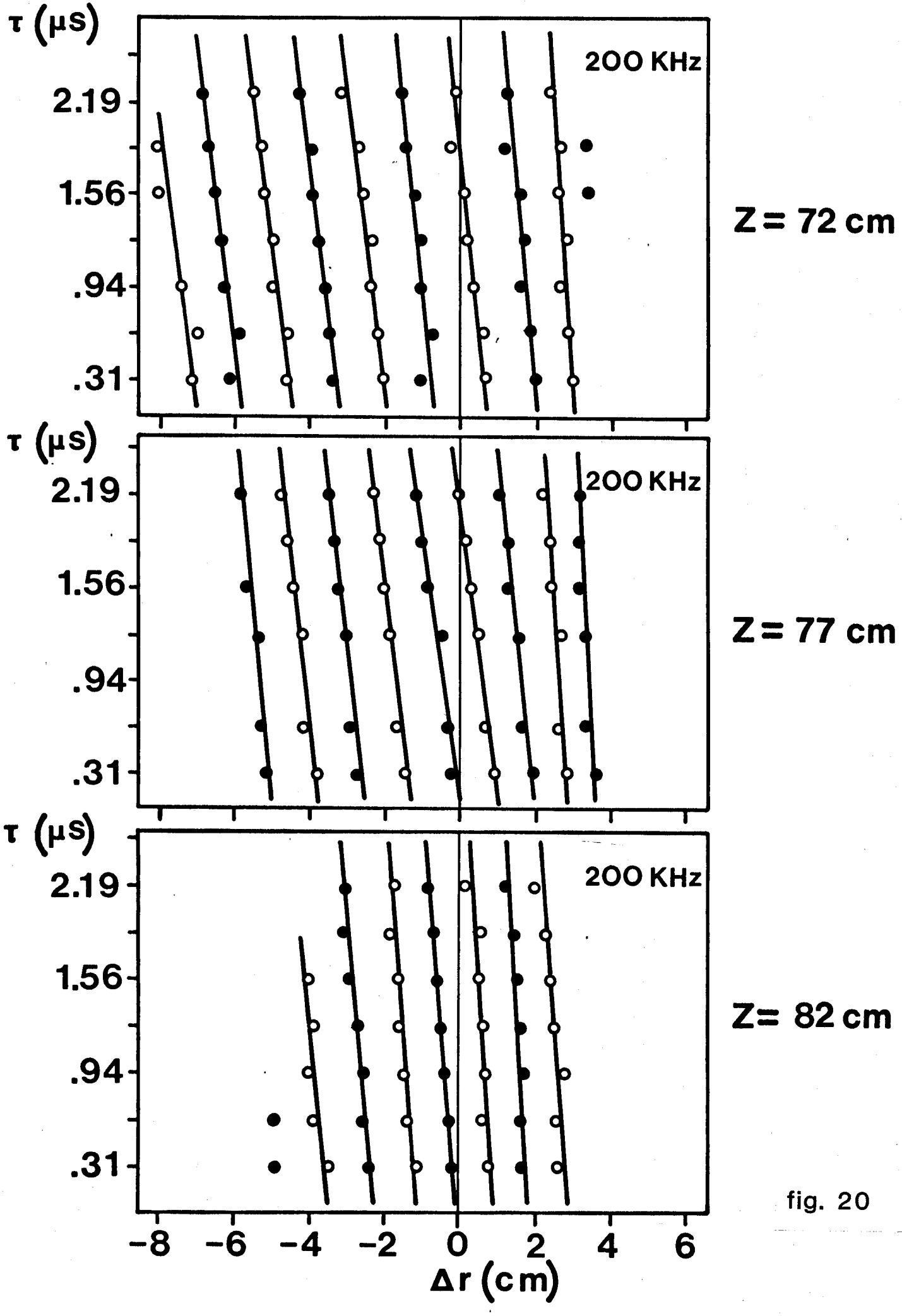
τ (μs)
2.19
1.56
.94
.31
200 KHz
Z = 72 cm
τ (μs)
2.19
1.56
.94
.31
200 KHz
Z = 77 cm
τ (μs)
2.19
1.56
.94
.31
200 KHz
Z = 82 cm
-8
-6
-4
-2
0
2
4
6
Δr (cm)

fig. 20

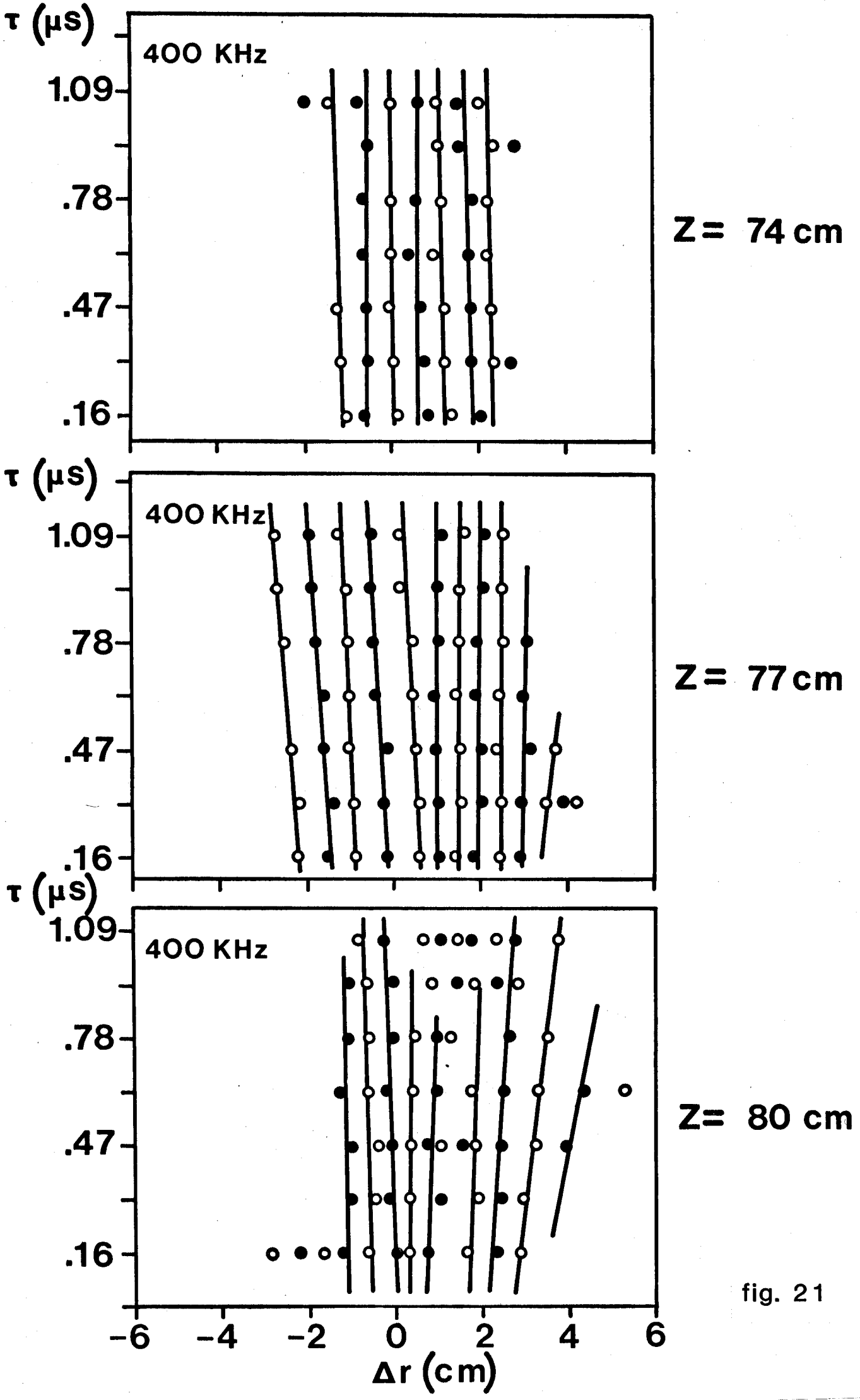
τ (μs)
400 KHz
1.09
.78
.47
.16
Z = 74 cm
τ (μs)
400 KHz
1.09
.78
.47
.16
Z = 77 cm
τ (μs)
400 KHz
1.09
.78
.47
.16
Z = 80 cm
-6
-4
-2
0
2
4
6
Δr (cm)

fig. 21

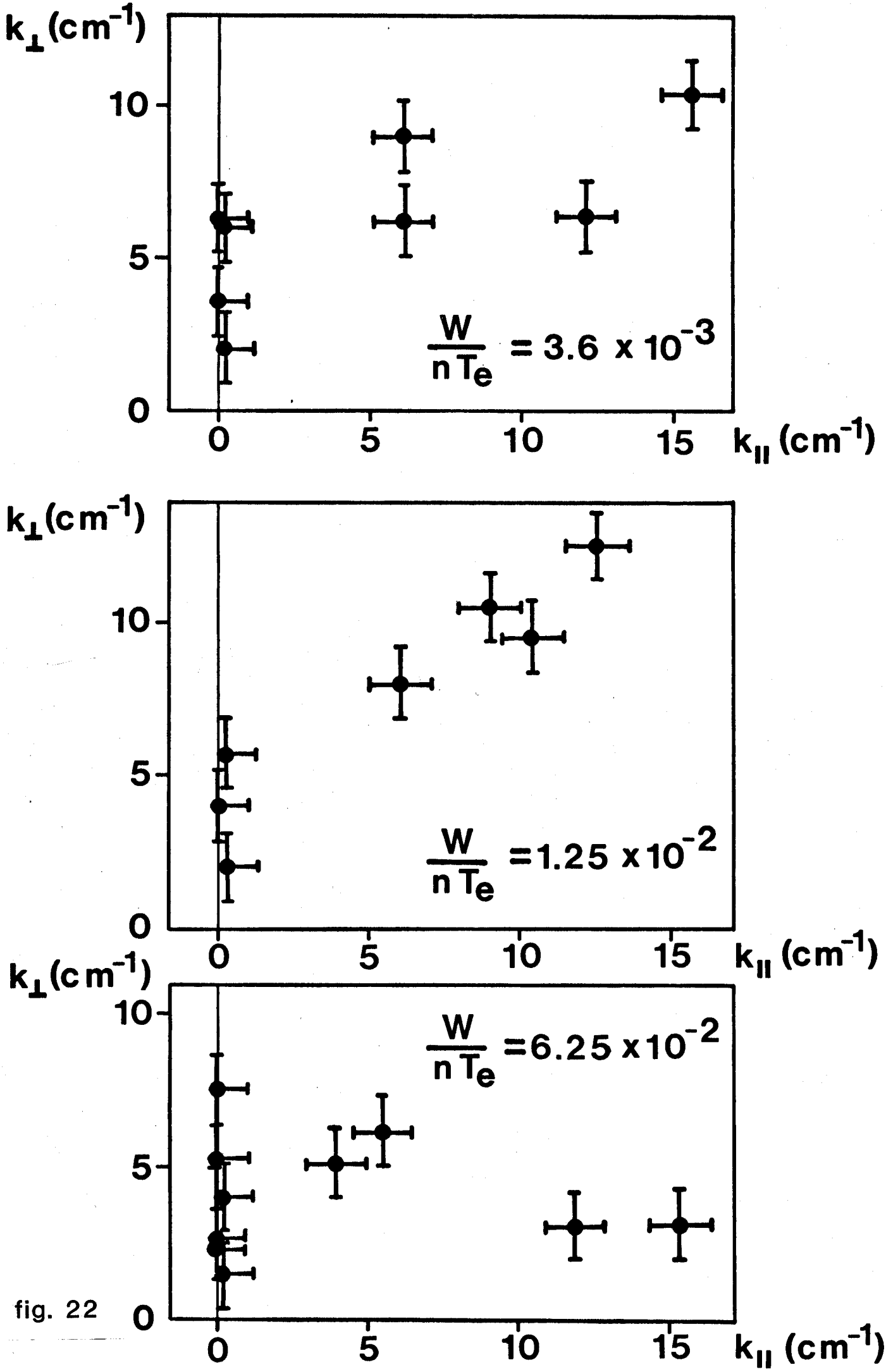
$k_\perp (cm^{-1})$
10
5
0
0
5
10
15
$k_{II} (cm^{-1})$
$\frac{W}{nT_e} = 3.6 \times 10^{-3}$
$k_\perp (cm^{-1})$
10
5
0
0
5
10
15
$k_{II} (cm^{-1})$
$\frac{W}{nT_e} = 1.25 \times 10^{-2}$
$k_\perp (cm^{-1})$
10
5
0
0
5
10
15
$k_{II} (cm^{-1})$
$\frac{W}{nT_e} = 6.25 \times 10^{-2}$

fig. 22

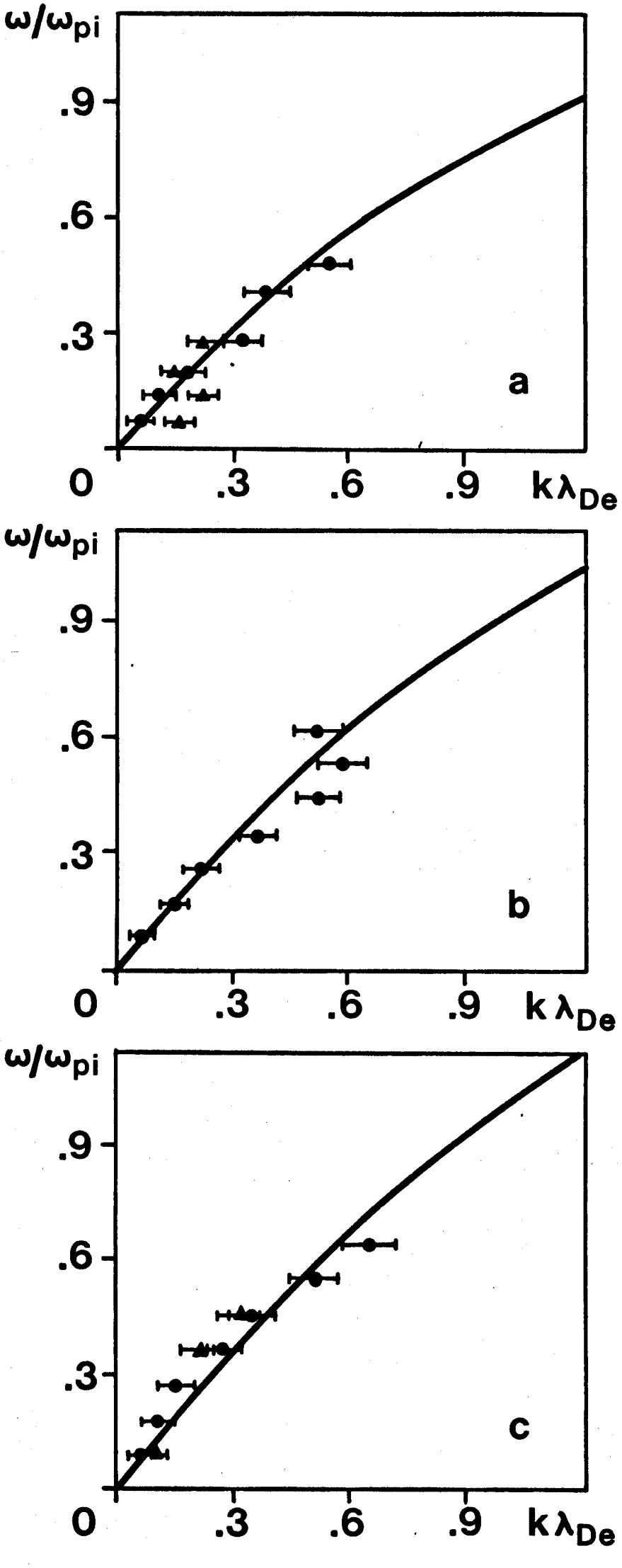

fig. 23

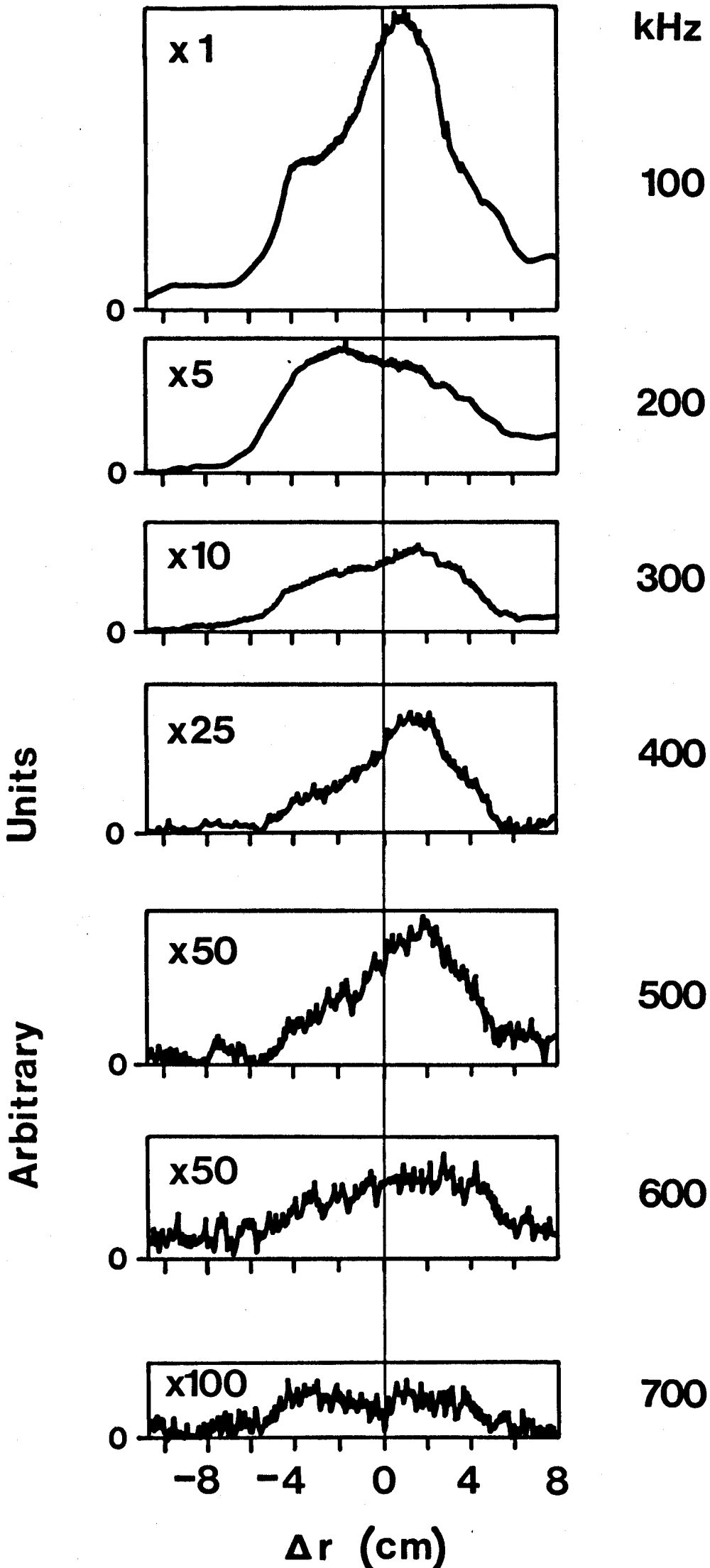
x1
x5
x10
x25
x50
x50
x100
0
kHz
100
200
300
400
500
600
700
Units
Arbitrary
-8
-4
0
4
8
Δr (cm)

fig. 24

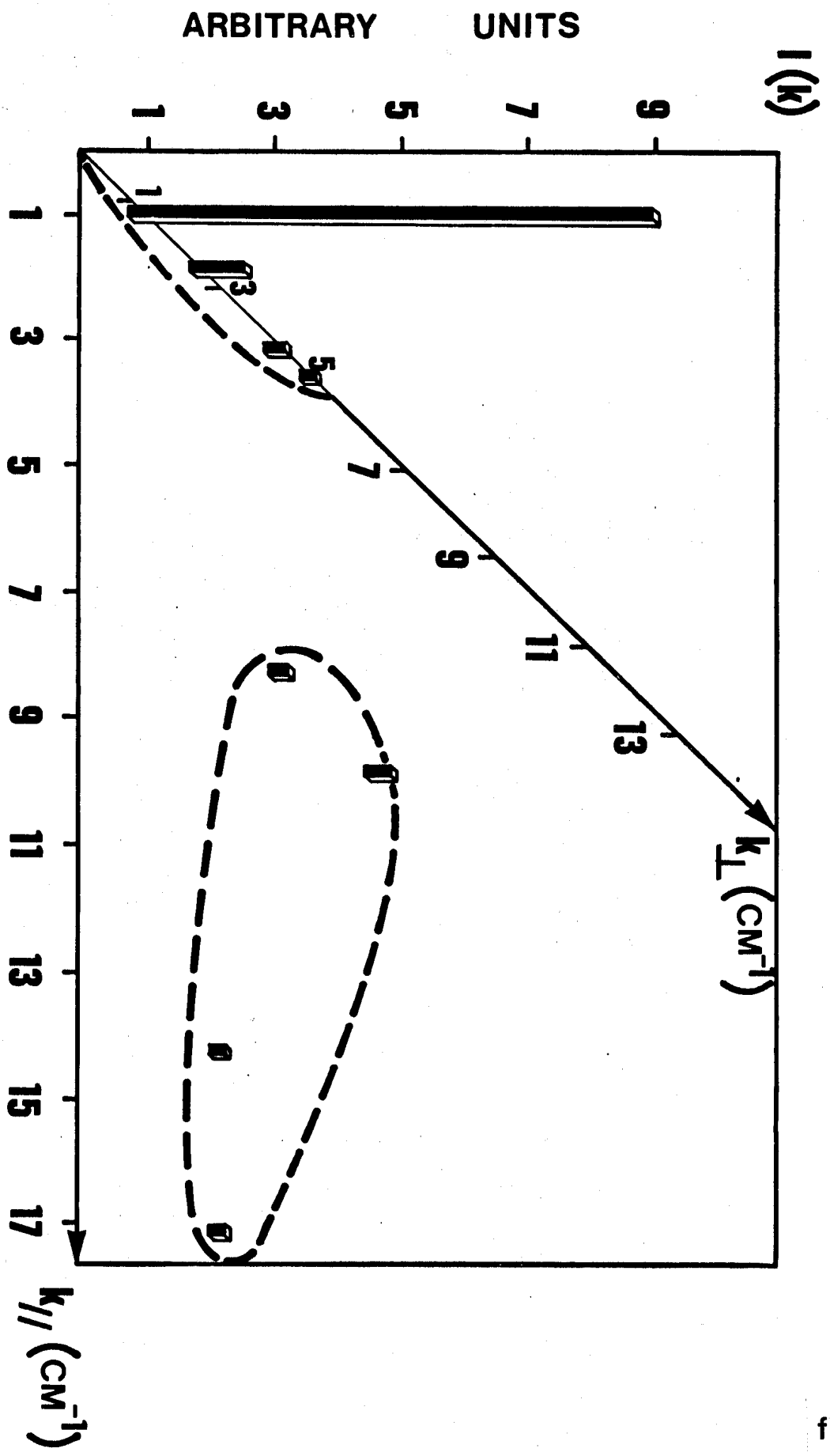
ARBITRARY UNITS
I(k)
1
3
5
7
9
1
3
5
7
9
11
13
15
17
1
3
5
7
6
11
13
$k_\perp$ (CM^{-1})
$k_{//}$ (CM^{-1})

fig. 25